Atmos. Chem. Phys. Discuss., 12, 5107–5188, 2012
www.atmos-chem-phys-discuss.net/12/5107/2012/
doi:10.5194/acpd-12-5107-2012

Atmospheric Chemistry and Physics Discussions

Aerosol-induced changes in summer rainfall and circulation in the Australasian region: a study using single-forcing climate simulations

L. D. Rotstayn[1], S. J. Jeffrey[2], M. A. Collier[1], S. M. Dravitzki[1], A. C. Hirst[1], J. I. Syktus[2], and K. K. Wong[2]

[1]Centre for Australian Weather and Climate Research, CSIRO Marine and Atmospheric Research, Aspendale, Vic, Australia
[2]Queensland Climate Change Centre of Excellence, Dutton Park, Qld, Australia

Received: 27 January 2012 – Accepted: 6 February 2012 – Published: 15 February 2012

Correspondence to: L. D. Rotstayn (leon.rotstayn@csiro.au)

Published by Copernicus Publications on behalf of the European Geosciences Union.

Abstract

We use a coupled atmosphere-ocean global climate model (CSIRO-Mk3.6) to investigate the roles of different forcing agents as drivers of summer rainfall trends in the Australasian region. Our results suggest that anthropogenic aerosols have contributed to the observed multi-decadal rainfall increase over north-western Australia.

As part of the Coupled Model Intercomparison Project Phase 5 (CMIP5), we performed multiple 10-member ensembles of historical climate change, which are analysed for the period 1951–2010. The historical runs include ensembles driven by "all forcings" (HIST), all forcings except anthropogenic aerosols (NO_AA) and forcing only from long-lived greenhouse gases (GHGAS). Anthropogenic aerosol-induced effects in a warming climate are calculated from the difference of HIST minus NO_AA. We also compare a 10-member 21st century ensemble driven by Representative Concentration Pathway 4.5 (RCP4.5).

Simulated aerosol-induced rainfall trends over the Indo-Pacific region for austral summer and boreal summer show a distinct contrast. In boreal summer, there is a southward shift of equatorial rainfall, consistent with the idea that anthropogenic aerosols have suppressed Asian monsoonal rainfall, and caused a southward shift of the local Hadley circulation. In austral summer, the aerosol-induced response more closely resembles a westward shift and strengthening of the upward branch of the Walker circulation, rather than a coherent southward shift of regional tropical rainfall. Thus the mechanism by which anthropogenic aerosols may affect Australian summer rainfall is unclear.

Focusing on summer rainfall trends over north-western Australia (NWA), we find that CSIRO-Mk3.6 simulates a strong rainfall decrease in RCP4.5, whereas simulated trends in HIST are weak and insignificant during 1951–2010. The weak rainfall trends in HIST are due to compensating effects of different forcing agents: there is a significant decrease in GHGAS, offset by an aerosol-induced increase in HIST minus NO_AA. However, the magnitude of the observed NWA rainfall trend is not captured by

ACPD
12, 5107–5188, 2012

the ensemble mean of HIST minus NO_AA, or by 440 unforced 60-yr trends calculated from a 500-yr pre-industrial control run. This suggests that the observed trend includes both a forced and unforced component.

We investigate the mechanism of simulated and observed NWA rainfall changes by exploring changes in circulation over the Indo-Pacific region. The key circulation feature associated with the rainfall increase is a lower-tropospheric cyclonic circulation trend off the coast of NWA. In the model, it induces moisture convergence and upward motion over NWA. The cyclonic anomaly is present in trends calculated from HIST minus NO_AA and from reanalyses.

Further analysis suggests that the cyclonic circulation trend in HIST minus NO_AA may be initiated as a Rossby wave response to positive convective heating anomalies south of the equator during November, when the aerosol-induced response of the model over the Indian Ocean still resembles that in boreal summer (i.e. a southward shift of equatorial rainfall). The aerosol-induced enhancement of the cyclonic circulation and associated monsoonal rainfall becomes progressively stronger from December to March, suggesting that there is a positive feedback between the source of latent heat (the Australian monsoon) and the cyclonic circulation.

CSIRO-Mk3.6 indicates that anthropogenic aerosols may have masked greenhouse gas-induced changes in rainfall over NWA and in circulation over the wider Indo-Pacific region: simulated trends in RCP4.5 resemble a stronger version of those in GHGAS, and are very different from those in HIST. Further research is needed to better understand the mechanisms and the extent to which these findings are model-dependent.

1 Introduction

Aerosols are known to affect climate via direct and indirect effects on radiation. These effects are thought to be large but very uncertain, especially the indirect effects, whereby aerosols modify the albedo and lifetime of clouds. According to Forster et al. (2007), the best estimate for the global-mean net anthropogenic aerosol forcing (including direct effects and the cloud-albedo effect) is $-1.2\,\mathrm{W\,m^{-2}}$, which is almost half

ACPD
12, 5107–5188, 2012

the magnitude of the positive radiative forcing of 2.6 $W m^{-2}$ from long-lived greenhouse gases (GHGs). Thus, aerosols are understood to substantially mask the effects of GHG-induced warming on global-mean temperature. Because concentrations of anthropogenic aerosols are projected to decrease during the next few decades, the associated "unmasking" is likely to exacerbate the increase of global-mean temperature (Kloster et al., 2010). Further, the hydrological sensitivity (defined as the change in global-mean precipitation per unit change in temperature) is thought to be higher for aerosols than for GHG-induced changes (Liepert et al., 2004; Kloster et al., 2010).

In addition to these globally averaged effects, there are large climatic effects due to strong spatial variations in the distribution of aerosols. This spatial inhomogeneity can cause large changes in atmospheric circulation and rainfall, especially in the tropics, where the circulation is known to be sensitive to horizontal temperature gradients (Rotstayn and Lohmann, 2002a). This can be referred to as the "dynamic" effect of aerosol forcing (Ming and Ramaswamy, 2011).

Recent research has also identified an important "thermodynamic" effect of anthropogenic aerosols on circulation and rainfall (Ming and Ramaswamy, 2011; Bollasina et al., 2011). This argument suggests that, regardless of the spatial pattern of forcing, the cooling effects of aerosols counter the GHG-induced weakening of tropical circulation. The latter is driven by the difference between rapidly increasing lower-tropospheric water vapour in a warming climate, and the precipitation rate, which increases more slowly (Knutson and Manabe, 1995; Held and Soden, 2006; Vecchi and Soden, 2007). The GHG-induced weakening is thought to act more strongly on the zonally asymmetric (Walker) circulation than on the zonally symmetric (Hadley) circulation (Vecchi and Soden, 2007). By implication, the same would apply to the thermodynamic effect of anthropogenic aerosols. Vecchi et al. (2006) analysed observations of sea-level pressure and found that the Pacific Walker circulation has indeed weakened since the mid-19th century. However, some studies based on satellite retrievals (Chen et al., 2002; Wentz et al., 2007) suggest that tropical circulation has strengthened in recent decades, reinforcing the point that these are unresolved research issues.

ACPD
12, 5107–5188, 2012

Early modelling of these effects generally used atmospheric global climate models (GCMs) coupled to very simple "slab" ocean models, in which oceanic heat transports are prescribed (e.g. Rotstayn et al., 2000b; Williams et al., 2001; Roberts and Jones, 2004; Kristjánsson et al., 2005). However, these models cannot capture the effects of changes in ocean dynamics, or the transient nature of climate change induced by aerosols (or any other forcing agent). For this reason, there has been an increasing trend in recent years to use fully coupled atmosphere-ocean GCMs (AOGCMs) to investigate these effects, even though they are much more complex and computationally expensive than atmospheric GCMs. For example, there have been several studies with AOGCMs of the effects of anthropogenic aerosols on the South Asian monsoon (Ramanathan et al., 2005; Meehl et al., 2008; Bollasina et al., 2011) and on rainfall in the Sahel (Kawase et al., 2010; Ackerley et al., 2011). Arblaster and Meehl (2006) used a similar approach to determine the contributions of different forcing agents to changes in the Southern Annular Mode. Using a low-resolution AOGCM, Rotstayn et al. (2007) investigated the effects of aerosol direct and indirect forcing on Australian rainfall. With a different focus, Roeckner et al. (2006) compared 21st century projections with two different assumptions about future emissions of carbonaceous aerosols, and found a marked sensitivity of the climate response over central Africa. To be effective, this approach generally requires substantial ensembles of simulations in which the effects of different forcing agents are treated individually, which further increases the computational expense.

Phase five of the Coupled Model Intercomparison Project (CMIP5) is currently in progress, and will continue through 2013. The CMIP5 experimental design (Taylor et al., 2009, 2012) does include provision for historical runs driven by individual forcing agents, but these are designated as "tier 2", the lowest priority of the three sets of experiments (Taylor et al., 2009, their Table 7). However, the importance of these simulations has increasingly been recognised, and efforts are underway to ensure that a substantial number of groups contribute such simulations to the CMIP5 data archive (e.g. Boucher et al., 2011).

ACPD
12, 5107–5188, 2012

Over the last few decades, there has been a significant rainfall increase over north-western Australia (NWA). Figure 1 shows observed December to March (DJFM) rainfall trends from the Australian Water Availability Project (AWAP; Jones et al., 2009) for December 1950 to March 2010. (Hereafter, we refer to this period as 1951–2010 when showing results for DJFM.) Although there is some evidence of a significant drying trend over limited parts of eastern Australia, the dominant feature is increasing rainfall over the north-west and centre of the continent. Over this region, most of the rainfall occurs in summer, and the cause of the trend may be policy-relevant for decisions regarding agriculture, mining infrastructure and regional communities.

A few authors have sought explanations for this trend, with no clear consensus emerging as yet. The first attempt was by Wardle and Smith (2004), who simulated a rainfall increase over northern Australia by decreasing surface albedo over the continent, though the prescribed decreases were much larger than could be justified based on current knowledge. Recognising the idealised nature of their experiment, the authors left the cause of the rainfall increase as an open question.

Rotstayn et al. (2007) used a low-resolution (spectral R21) version of the CSIRO GCM ("Mk3A") to perform ensembles of coupled ocean-atmosphere simulations for the period 1871–2000, with and without changes in anthropogenic aerosols. They found that inclusion of anthropogenic aerosol forcing gave a rainfall response similar to the observed increase over NWA. They attributed this to a change in the meridional temperature gradient induced by aerosols from the Asian region. However, they also expressed a number of reservations about their results, including simplified and uncertain treatments of aerosol processes, a lack of agreement between modelled and observed rainfall trends in other parts of Australia, and a poor simulation of variability associated with the El Niño-Southern Oscillation (ENSO) in their low-resolution model.

The issue of ENSO-related variability in CSIRO Mk3A was taken up in more detail by Shi et al. (2008). They pointed out that the low-resolution model suffers from an equatorial Pacific cold-tongue bias, with the effect that the sea surface temperature (SST) anomalies associated with ENSO extend too far west into the eastern Indian Ocean.

ACPD
12, 5107–5188, 2012

Consequently, in austral summer ENSO-related rainfall variability over Australia was also shifted westward, from north-eastern Australia towards NWA. The cold-tongue bias is a long-standing problem in coupled AOGCMs (Latif et al., 2001), which suggests that other models will also be affected to varying degrees.

Cai et al. (2011b) revisited the question using 24 models from CMIP3. They found that only nine models produce a statistically significant increasing rainfall trend over NWA, and all were much weaker than the observed trend for 1950–2008. They then grouped the models according to whether they treated both direct and indirect anthropogenic aerosol effects, or direct effects only, and found little difference between the two groups. They concluded that increasing anthropogenic aerosols in the multi-model ensemble play a negligible role in generating the observed rainfall increase over NWA. They also found that projected 21st century rainfall changes over NWA were highly variable among the models, with a mixture of both positive and negative changes. Note that this implies that the response of NWA rainfall to increasing long-lived GHGs is highly variable among the CMIP3 models, so it is also likely that the response to anthropogenic aerosol forcing (which is much more uncertain and spatially inhomogeneous) will be highly variable. Aside from the very simplified aerosol treatments in many CMIP3 models, this may explain why Cai et al. (2011b) were unable to detect a clear anthropogenic aerosol signal. However, the lack of individual-forcing simulations in the CMIP3 data set makes it difficult to draw firm conclusions.

Several other studies have investigated aspects of the NWA rainfall increase. Zhang (2010) found that the observed significant increase in NWA summer rainfall corresponds to earlier onset and duration of the monsoon, rather than an increase in intensity of rainfall events. Luffman et al. (2010) evaluated the response of an atmospheric GCM forced by observed changes in SST in the Indian and Pacific Oceans (both separately and together). They found that none of the experiments simulated an east-west pattern of rainfall trend over Australia that resembled the observed trends. They suggested that while the drying trend in the east may be partially explained by changes in the tropical Indian and Pacific SST, increasing rainfall in the north-west must be related

ACPD
12, 5107–5188, 2012

to other factors. Berry et al. (2011) examined the synoptic-scale processes associated with rainfall events in NWA. They found that prior to rain falling in the interior of NWA, there is a shift in the origins of low-level air parcels, such that air is advected from the tropical maritime regions, rather than from over the continent. They also suggested that the observed increase in rainfall may be primarily linked to changes in synoptic weather systems, rather than changes in the state of the ocean. Recently, Lin and Li (2012) used reanalysis data to show that an increasing trend in atmospheric ascent induced by a warming SST trend in the tropical Atlantic may partially explain the observed rainfall trend in NWA. Their suggested mechanism involves a Rossby wave train that travels eastward, embedded in the westerly jet waveguide of the Southern Hemisphere.

Another relevant study was by Zhang and Zhang (2010), who pointed out a positive correlation (on inter-annual time scales) between the Australian monsoon and the East Asian winter monsoon. Although their focus was not on long-term rainfall trends, they suggested that variations in cross-equatorial flow and the upward branch of the Hadley circulation create an important link between the two monsoons.

Here we use individual-forcing experiments with a coupled AOGCM to investigate the cause of recent Australian summer rainfall trends, and in particular, whether there is a link to forcing from anthropogenic aerosols. The individual-forcing simulations used in this study comprise part of a CMIP5 submission with the CSIRO Mark 3.6 (CSIRO-Mk3.6) GCM; the submission was a collaborative effort between The Queensland Climate Change Centre of Excellence (QCCCE) and the Commonwealth Scientific and Industrial Research Organisation (CSIRO). The model is described in Sect. 2, and the forcing and simulations are described in Sect. 3. Results and discussion are in Sect. 4; there, we consider Australian summer rainfall changes (especially over NWA), how they relate to changes in circulation over the wider Indo-Pacific region, and whether there is a link to anthropogenic aerosol forcing.

ACPD
12, 5107–5188, 2012

2 Model description

2.1 Overview

The CSIRO Mark 3.6 (CSIRO-Mk3.6) GCM was developed from the earlier Mk3.5 version, which was described in detail by Gordon et al. (2002, 2010). It is a coupled atmosphere-ocean model with dynamic sea ice. It also has a soil-canopy scheme with prescribed vegetation properties. The ocean, sea-ice and soil-canopy models are unchanged between Mk3.5 and Mk3.6. The main differences between Mk3.5 and Mk3.6 are the inclusion of an interactive aerosol treatment and an updated radiation scheme in Mk3.6. Rotstayn et al. (2010) gave an overview of CSIRO-Mk3.6; they also assessed the model's simulation of Australian mean climate and natural rainfall variability associated with ENSO, with generally favourable conclusions. Here, we briefly describe the main components of the model, with more detail about the aerosol and radiation treatments in Sect. 2.2.

The atmospheric component is a spectral model, which utilizes the flux form of the dynamical equations (Gordon, 1981). It has 18 vertical levels and horizontal resolution of approximately $1.875^{\circ} \times 1.875^{\circ}$ (spectral T63). Advection of water vapour, cloud water and trace quantities is not treated spectrally; vertical advection is handled using a flux-corrected transport scheme (Van Leer, 1977), and horizontal advection is handled using a semi-Lagrangian scheme (McGregor, 1993).

The main aspects of the atmospheric physics package (other than radiation and aerosols) are as follows. Convection is treated using the mass-flux scheme of Gregory and Rowntree (1990), modified by the inclusion of downdrafts (Gregory, 1995). The treatment of surface fluxes and vertical turbulent mixing is based on stability-dependent K-theory (Louis, 1979). Under convective conditions, an additional non-local countergradient flux is added in the boundary layer (Holtslag and Boville, 1993); this feature was not included in Mk3.5. The stratiform cloud and precipitation scheme was described by Rotstayn (1997, 1998), with an improved treatment of mixed-phase clouds as in Rotstayn et al. (2000a). The scheme includes a simple parameterization of

ACPD
12, 5107–5188, 2012

fractional cloudiness, prognostic variables for cloud liquid water and cloud ice, and physically distinct treatments of warm-rain and frozen-precipitation processes. Interactions between the cloud and aerosol schemes are described in Sect. 2.2.

The ocean model is based on version 2.2 of the Modular Ocean Model (MOM2.2; Pacanowski, 1996). Every atmospheric grid-box is coupled to two oceanic grid-boxes: enhanced north-south resolution in the ocean model was implemented with the aim of improving the representation of tropical variability. The ocean model thus has resolution of approximately $0.9375^{\circ} \times 1.875^{\circ}$ and has 31 vertical levels. Several improved physical parameterizations were implemented in Mk3.5 to reduce biases and climate drift in the earlier Mk3.0 version (Gordon et al., 2002, Fig. 22). In particular, the ocean model was upgraded to include spatially varying eddy-transfer coefficients (Visbeck et al., 1997) and a revised parameterization of mixed-layer depth (Kraus and Turner, 1967). Changes to the ocean-atmosphere coupling included an improved river-routing scheme, with time-delay due to flow (Gordon et al., 2010). The sea-ice model is based on O'Farrell (1998), with revised numerics as described by Gordon et al. (2010).

2.2 Interactive aerosol scheme

There are 11 prognostic mass tracers in the aerosol scheme: dimethyl sulfide (DMS), sulfur dioxide (SO_2), sulfate, hydrophobic and hydrophilic forms of black carbon (BC) and organic carbon, and four size bins of mineral dust, with radii ranging from 0.1–1, 1–2, 2–3 and 3–6 µm respectively. A factor of 1.3 is used to convert the mass of organic carbon to the mass of organic aerosol (OA) (Penner et al., 1998). Number concentrations of two modes of sea salt (film-drop and jet-drop) are diagnosed as a function of 10-m wind speed in the marine boundary layer (O'Dowd et al., 1997), but are not treated prognostically. Also, the distribution of stratospheric sulfate from volcanic eruptions is prescribed using monthly mean data (extended from Sato et al., 1993).

Prescribed anthropogenic and biomass-burning sources of sulfur, BC and OA are based on the recommended data sets for CMIP5 (Lamarque et al., 2010), with some

ACPD
12, 5107–5188, 2012

modifications. We uniformly increased the emissions of BC (by 25 %) and OA (by 50 %) to improve the agreement between modelled and observed fields of carbonaceous aerosol. Similar adjustments were applied in earlier versions of the model (Rotstayn et al., 2007, 2010). We justified this by the large uncertainty in emissions of carbonaceous aerosol (Bond et al., 2004), and the standard inventory's omission of anthropogenic secondary organic aerosol (SOA), which can substantially enhance effective emissions of OA (Kanakidou et al., 2005; Lee et al., 2008). The relatively small emissions of black carbon from aviation were omitted from our simulations. With these adjustments, the annual emission of BC in the year 2000 is 9.7 Tg (compared to 7.7 Tg in the standard inventory), and the emission of OA from anthropogenic and biomass-burning sources is 53 Tg C (compared to 35 Tg C in the standard inventory).

Prescribed natural sources of sulfur comprise SO_2 from continuously erupting volcanoes (8.0 Tg S yr^{-1}) and biogenic emissions of DMS from oceans, soils and plants (0.9 Tg S yr^{-1}) (Rotstayn and Lohmann, 2002b). The oceanic DMS source is calculated from a global database of DMS measurements, and is thus representative of modern-day climate (Kettle et al., 1999; Kettle and Andreae, 2000). The DMS flux parameterization is based on the quadratic relation from Nightingale et al. (2000) for wind speeds below 13 m s^{-1} and the piecewise-linear relation from Liss and Merlivat (1986) for wind speeds above 18 m s^{-1}, with a linear transition between them at wind speeds from 13 to 18 m s^{-1}. A parameterization of sub-grid gustiness due to deep convection and free convection is included, analogous to that used in the dust scheme (Rotstayn et al., 2011). With these treatments, the global oceanic DMS source is 27 Tg S yr^{-1} in 2000, which is larger than the source of 18 Tg S yr^{-1} prescribed for the AeroCom models (Dentener et al., 2006). However, an updated DMS database (Lana et al., 2011) indicates that global DMS emissions are larger than previously thought, with a best estimate of 28.1 Tg S yr^{-1}, so the emissions in our model may not be excessive.

The prescribed climatological source of natural SOA assumes rapid conversion to OA of a fixed percentage of the terpene emission from Guenther et al. (1995); earlier versions of the model assumed a yield of 13 %, giving a global source of 16.4 Tg C per

ACPD
12, 5107–5188, 2012

annum. In view of evidence that this may seriously underestimate global production of biogenic SOA (Kanakidou et al., 2005; Goldstein and Galbally, 2007), the yield was increased to 28 %, corresponding to a global source of 35 Tg C. However, recent work by Pye et al. (2010) suggests that this may be an overestimate: using a global chemical transport model, they estimated that 14–15 Tg yr^{-1} of SOA is formed from terpenes and 8–9 Tg yr^{-1} from isoprene, for a total yield of 22–24 Tg yr^{-1} of biogenic SOA.

The treatment of mineral dust emission follows Ginoux et al. (2001, 2004). The scheme is based on satellite retrievals from the Total Ozone Monitoring Spectrometer (TOMS), which indicate that most large dust sources correspond to topographic depressions (Prospero et al., 2002). Further details of the dust scheme are given by Rotstayn et al. (2011), who obtained global dust emissions of 3569 Tg for the year 2000. This is somewhat larger than the range of 1000 to 3000 Tg yr^{-1} that was found to be consistent with observations by Cakmur et al. (2006). Rotstayn et al. (2011) attributed the relatively large dust emission to the model's implementation of a sub-grid gustiness parameterization, and noted that this was the likely cause of a global dust burden close to the high end of the range found in other dust models.

Treatments of aerosol transformations are limited to oxidation reactions involving sulfate precursors, and a simple time-dependent decay of hydrophobic carbonaceous aerosols to their respective hydrophilic forms. The treatment of tropospheric sulfur chemistry is based on Feichter et al. (1996), with modifications as in Rotstayn and Lohmann (2002b). The carbonaceous aerosol module (Cooke et al., 1999) assumes a fixed e-folding time of 1 day for the conversion of BC and OA from their hydrophobic to hydrophilic forms.

Tracer transport occurs by advection, vertical turbulent mixing and vertical transport inside deep convective clouds. The treatments of advection and vertical turbulent mixing were described in Sect. 2.1. Convective tracer transport is based on the vertical profiles of the updraft mass flux and compensating subsidence generated by the convection scheme (Gregory and Rowntree, 1990); further details are given by Rotstayn and Lohmann (2002b).

ACPD
12, 5107–5188, 2012

Prognostic aerosols are removed from the atmosphere by wet and dry deposition, and (for dust) by gravitational settling. Wet deposition processes include in-cloud and below-cloud scavenging by rain and snow (Rotstayn and Lohmann, 2002b). Dry deposition processes follow Lohmann et al. (1999) for sulfate, SO_2 and carbonaceous aerosol. The treatments of dry deposition and gravitational settling of dust follow Ginoux et al. (2001).

2.3 Radiation and indirect aerosol effects

The aerosol treatments in CSIRO-Mk3.6 are supported by an updated radiation scheme that can treat aerosol-radiative effects (which was not possible in Mk3.5). The radiation scheme includes the shortwave effects of all the above aerosol types and the longwave effects of dust and stratospheric aerosol. Further details of the aerosol optical properties are given by Rotstayn et al. (2007), with updates to the dust treatment described by Rotstayn et al. (2011). The shortwave radiation scheme is a two-stream code with 12 bands and 24 k terms (Grant and Grossman, 1998; Grant et al., 1999). The longwave scheme has 10 bands – a combination of k distribution and pre-computed transmittances (Grant et al., 1999; Chou and Lee, 2005). Another advantage of the new radiation scheme is the ability to treat non-CO_2 GHGs (methane, nitrous oxide and halocarbons), avoiding the need for the "equivalent CO_2" approximation that was used in Mk3.5.

The model also includes treatments of aerosol indirect effects on liquid-water clouds. The parameterisation of cloud droplet number concentration (N_d, in m^{-3}) is based on the relation from Jones et al. (1994), namely

$$N_d = \max\{375 \times 10^6 (1 - e^{-2.5 \times 10^{-9} A}), N_{min}\}, \quad (1)$$

where $N_{min} = 10 \times 10^6$ and A is the number concentration of hydrophilic aerosols (in m^{-3}). In the radiation scheme, carbonaceous aerosols (OA and BC) are assumed to exist as an internal mixture, and all other aerosol species are externally mixed; for

ACPD
12, 5107–5188, 2012

consistency, this assumption is also applied to the calculation of N_d. Thus A is taken as the sum of the concentrations of sulfate, sea salt and hydrophilic carbonaceous aerosol. The conversion from aerosol mass concentration m_s (carried prognostically by the model) to aerosol number A_s for sulfate and carbonaceous aerosol is based on the same (prescribed) mass-number relationship that is used for that species in the radiation scheme. Thus if m_s and m_c are respectively the mass concentrations of sulfate and hydrophilic carbonaceous aerosol (OA plus BC) in kg m^{-3}, $A = 5.1 \times 10^{17} m_s + 3.0 \times 10^{17} m_c$. The windspeed-dependent diagnostic relation for sea salt in the marine boundary layer provides number concentrations of sea salt (O'Dowd et al., 1997), so no conversion is necessary.

Equation (1) feeds into the calculation of cloud droplet effective radius, which includes a parameterization of the observed increase of droplet spectral dispersion with increasing N_d (Rotstayn and Liu, 2009). In stratiform clouds, Eq. (1) also feeds into the calculation of drizzle formation ("autoconversion"; Rotstayn and Liu, 2005), which affects the persistence of liquid water clouds (the so-called second indirect effect). The autoconversion scheme also includes a simple parameterization of sub-grid cloud-water variability, whereby only the part of the grid box in which the cloud liquid-water content exceeds the autoconversion threshold is used in the calculation of autoconversion (Rotstayn, 2000); one effect of this parameterization is to reduce the magnitude of the simulated second indirect effect, for a given treatment of the autoconversion rate and threshold.

The aerosol treatments in our model are simplified in many respects. For example, a limitation of the single-moment scheme is that different aerosol modes cannot interact (e.g. by coagulation or heterogeneous chemistry). Parameterization of cloud droplet number concentration as an empirical function of aerosol number ignores much of the subtle physics and chemistry of cloud droplet nucleation. These and other limitations are discussed in more detail by Rotstayn et al. (2007). Having said that, similar simplifications are adopted in many current GCMs, due to the long time integrations and multiple ensembles that are needed for climate studies.

ACPD
12, 5107–5188, 2012

3 Forcing and simulations

3.1 Prescribed data sets

Our simulations are based on the CMIP5 experimental design (Taylor et al., 2009, 2012); see http://cmip-pcmdi.llnl.gov/cmip5/ for further information about CMIP5 forcing data. Anthropogenic forcing agents in our runs are long-lived GHGs, ozone and aerosols. (Changes in land use are not included.) We prescribed CMIP5-recommended, annual-mean concentrations of long-lived GHGs (carbon dioxide, methane, nitrous oxide and chlorofluorocarbons), and monthly mean, spatially varying ozone concentrations. Ozone concentrations are based on the AC&C/SPARC ozone database (Cionni et al., 2011); they are three dimensional in the troposphere, and zonally averaged in the stratosphere. Emissions of anthropogenic aerosols and aerosol precursors also follow CMIP5 recommendations (Lamarque et al., 2010), with modifications as described in Sect. 2. In addition to direct effects and indirect aerosol effects on liquid-water clouds (Sect. 2), the model also includes a simple treatment of the effect of BC on snow albedo (Hansen and Nazarenko, 2004). The anthropogenic-forcing data sets are prescribed for both the historical period and the four Representative Concentration Pathways (RCPs); see Moss et al. (2010) for an overview of the RCPs. We also included the historical time series of annual-mean total solar irradiance recommended for CMIP5; this includes estimates of both the 11-yr solar cycle and changes in background irradiance (Lean, 2000; Wang et al., 2005).

CMIP5 does not specifically include a prescribed data set for volcanic forcing. We prescribed zonally averaged distributions of stratospheric sulfate based on Sato et al. (1993) (http://data.giss.nasa.gov/modelforce/strataer/); a recent update, which extended the data set beyond 1999, was not available at the time we commenced the simulations, so we set volcanic forcing to zero from 2000 onwards.

ACPD
12, 5107–5188, 2012

3.2 Aerosol forcing

Since our main focus in this paper is to compare the effects of anthropogenic aerosols and GHGs, in this section we discuss the magnitude and spatial pattern of aerosol forcing. We first summarise the global-mean aerosol burdens and aerosol optical depths.

Table 1 shows global-mean column burdens for the aerosol species treated by the model, for both 1850 and 2000. Also shown are reference ranges for the year 2000, based on one or more studies that have reviewed a range of models. The most notable feature of Table 1 is that the Mk3.6 column burdens of sulfate, OA and dust in 2000 are close to the top of their reference ranges.

A contributing factor to the relatively large sulfate burden in the year 2000 is the relatively large emission of DMS (27 Tg S yr^{-1}), but this also tends to increase the sulfate burden in 1850. The difference in the sulfate burden between 2000 and 1850 is 3.3 mg m^{-2}. This can be compared with Schulz et al. (2006), who found an average increase since preindustrial times of 2.12 mg m^{-2} in the AeroCom models (with a standard deviation of 0.82 mg m^{-2}) and an average increase in other studies of 2.70 mg m^{-2} (with a standard deviation of 1.09 mg m^{-2}).

The large OA burden for year-2000 is consistent with our large emissions of OA, in which both the anthropogenic emissions and natural SOA emissions were increased with respect to their default values. However, the relative change in OA burden from 1850 to 2000 is smaller than that obtained for sulfate and BC; this is due to the substantial contribution from SOA (which is unchanged between 1850 and 2000) and the relatively small difference between preindustrial and modern-day biomass-burning emissions in the inventory from Lamarque et al. (2010).

Although we also scaled-up the BC emissions, our global-mean BC column burden for 2000 is not especially large with respect to the reference range. This may reflect the fact that our BC emissions of 9.7 Tg yr^{-1} are still smaller than those assumed in some earlier studies, e.g. an average of 11.9 Tg yr^{-1} for the AeroCom models (Textor et al., 2006).

ACPD
12, 5107–5188, 2012

As mentioned above, the relatively large dust burden can be attributed to the strong effect of the sub-grid gustiness parameterization in the dust uplift scheme (Rotstayn et al., 2011). The sea-salt burden is close to the middle of the range of results from the AeroCom models.

In summary, the total modern-day aerosol burden in CSIRO-Mk3.6 is relatively large, but this is partly related to large emissions of natural aerosols (dust, SOA and sulfate derived from DMS) and a relatively small difference between preindustrial and modern-day biomass-burning emissions in the CMIP5 emission inventory. As discussed above for sulfate, the change between the preindustrial and modern-day burden is larger than average, but not outside the range of earlier studies.

The global-mean aerosol optical depth at 550 nm for the year-2000 simulation is 0.175. Consistent with the relatively large burdens of sulfate, OA and dust, this is somewhat higher than the global average suggested by a composite of satellite retrievals (~0.15) and by surface-based remote sensing (~0.135) (Kinne et al., 2006). Similarly, Remer et al. (2008) inferred a global-mean aerosol optical depth of 0.13 to 0.14 over oceans, and 0.19 over land from the Collection 5 Moderate Resolution Imaging Spectroradiometer (MODIS) aerosol products. Our global-mean aerosol optical depth at 550 nm in 1850 is 0.125, so the anthropogenic component (estimated as 2000 minus 1850) is 0.050. This is somewhat larger than an average of 0.029 in the AeroCom models, and an average of 0.041 found in other studies by Schulz et al. (2006).

With these aerosol treatments, the net top-of-atmosphere (TOA) anthropogenic aerosol radiative flux perturbation (RFP) from 1850 to 2000 is $-1.4\,\mathrm{W\,m^{-2}}$, diagnosed from the difference of net TOA radiation between the two 30-yr atmospheric runs with prescribed SSTs and sea-ice, as in the CMIP5 experimental design (Taylor et al., 2009). This represents the sum of direct and (first and second) indirect effects, plus the effect of BC on snow albedo. Our result is a little larger in magnitude than the best estimate of $-1.2\,\mathrm{W\,m^{-2}}$ from Forster et al. (2007), though it is well within the large uncertainty range. The RFP method is used because, once indirect effects other than the

ACPD
12, 5107–5188, 2012

cloud-albedo effect are considered, it is not feasible to calculate an instananeous forcing. Several studies have suggested that the RFP provides a satisfactory alternative to instantaneous forcing (Rotstayn and Penner, 2001; Hansen et al., 2002; Lohmann et al., 2010).

It is interesting to also consider the breakdown of aerosol forcing into direct and indirect effects, as well as spatial variations of the forcing. We calculated the direct and first indirect (cloud-albedo) effects as instantaneous forcings, using two pairs of five-year runs with prescribed SSTs and sea ice (similar to the approach used to calculate the RFP). However, instead of taking the change in net TOA radiation, instantaneous forcings were calculated using double calls to the shortwave radiation scheme, in the manner of Lohmann et al. (2010).

Figure 2a shows the direct aerosol forcing at the top of the atmosphere. The global-mean direct TOA forcing ($-0.25\,W\,m^{-2}$) is close to the best estimate of $-0.30\,W\,m^{-2}$ from Myhre (2009), who demonstrated consistency between a model and satellite-retrieved values. As expected in the presence of absorbing aerosols, the direct surface forcing in Fig. 2b is generally larger in magnitude than the TOA forcing; the difference ($1.53\,W\,m^{-2}$ in the global mean) represents atmospheric aerosol absorption. Some areas where the surface forcing is positive (e.g. over the south-eastern USA) occur because biomass-burning aerosol emissions in the inventory of Lamarque et al. (2010) are higher there in 1850 than in 2000. The pattern of the first indirect effect (Fig. 2c) shows some similarity to the direct effect, but there is a noticeable enhancement in regions of persistent low cloud cover, such as the eastern subtropics of the Pacific and Atlantic Ocean basins.

The total aerosol RFP at TOA is shown in Fig. 2d. Despite the noise, which is an intrinsic feature of the RFP method, the main spatial features of panels (a) and (b) are evident in panel (d). Possibly of relevance to the present study is that South and East Asia and the Indonesian region feature prominently, consistent with large emissions from these areas.

ACPD
12, 5107–5188, 2012

3.3 Transient simulations

As well as most of the "core" and "tier 1" CMIP5 experiments, we have performed a substantial set of 10-member individual-forcing historical ensembles (Experiments 7.2 and 7.3 in Taylor et al., 2009). These are designed to explore the effects of changes in GHGs, aerosols, ozone and natural (solar and volcanic) forcing. Here, we focus mainly on the following 10-member ensembles:

- HIST: standard historical run with "all forcings", namely, long-lived GHGs, ozone, anthropogenic aerosols, and natural forcing.
- NO_AA: same as HIST, but with anthropogenic and biomass-burning aerosol emissions fixed at 1850 levels. (We hereafter refer to these emissions collectively as "anthropogenic".)
- GHGAS: historical run forced only by changes in long-lived GHGs.
- RCP4.5: projection for 2006 to 2100 based on Representative Concentration Pathway 4.5, in which total radiative forcing is stabilized before 2100 at roughly 4.5 $W m^{-2}$ (Clarke et al., 2007).

Each historical run was initialized in January, 1850 from states taken from years 80 to 200 of a 500-yr preindustrial control run (piControl), at intervals of 10 to 17 yr. Each RCP4.5 run was initialized in January 2006 from the end of a run from the HIST ensemble. In principle, the CMIP5 historical period ends in 2005, but we extended all the historical runs from 2006 to 2012 by following the assumptions in RCP4.5. (Thus, the HIST ensemble is identical to RCP4.5 for 2006–2012). In the following analysis, we will calculate 60-yr trends from the historical runs (1951–2010) and 90-yr trends from RCP4.5 (2011–2100).

An addition to the above simulations (which are "core" for the purpose of this study) we will also show some results from the following additional ensembles:

ACPD
12, 5107–5188, 2012

– NAT: historical run forced only by changes in volcanic and solar forcing.

– NO_OZ: same as HIST, but with ozone concentrations fixed at 1949 levels from 1950 onwards.

– ASIA: same as NO_AA, except that "Asian" aerosol emissions are allowed to vary normally. Asia is defined as the region from 10° S to 45° N and from 65° E to 150° E.

We use the difference of HIST minus NO_AA to diagnose the aerosol-induced effect against a background of GHG-induced warming. There is evidence from earlier studies with slab ocean models that the response is non-linear, suggesting that HIST minus NO_AA is not identical to an experiment forced only by anthropogenic aerosols (Feichter et al., 2004; Ming and Ramaswamy, 2009). Similarly, the effects of changes in ozone (HIST minus NO_OZ) and Asian aerosols (ASIA minus NO_AA) are diagnosed from the differences of pairs of experiments.

Figure 3 shows anomalies of annual, global-mean near-surface temperature T_s from the model and observations from HadCRUT3 (Brohan et al., 2006). Observed global-mean T_s is mostly within the range of runs in the HIST ensemble, except for a period in the early 20th century. The observed T_s curve in Fig. 3 does not show the observational uncertainties, which are larger than ±0.2 °C prior to 1940 (Brohan et al., 2006). HIST slightly underestimates the observed warming towards the end of the 20th century, though the agreement is better between 2000 and 2010. In contrast, the GHGAS and NO_AA ensembles strongly overestimate the increase in T_s. NO_AA simulates slightly more warming than GHGAS, mainly due to changes in solar irradiance. After 2010, RCP4.5 simulates a rapid increase in T_s, due to increasing concentrations of long-lived GHGs and decreasing emissions of aerosols and aerosol precursors (Lamarque et al., 2010).

ACPD
12, 5107–5188, 2012

4 Results and discussion

4.1 Evaluation of mean state and variability

Before considering the rainfall trends in more detail, it is useful to briefly evaluate the model's simulation of rainfall and circulation in the Australian region. Rainfall, surface temperature and sea-level pressure for summer and winter were previously evaluated by Rotstayn et al. (2010), based on a control run of CSIRO-Mk3.6 with modern-day forcing, and different aerosol emissions from those used in CMIP5. Modelled and observed climatological rainfall for DJFM are compared in Fig. 4. The model has a tendency to be too wet in the far north, and too dry in the south-west, and the effects of topography in the south-east and in Tasmania are not well resolved. However, the broad pattern of Australian summer rainfall is simulated rather well.

Figure 5 shows the DJFM climatologies of horizontal winds at 850 hPa (vectors) and vertical pressure velocity at 500 hPa (shading) from the HIST ensemble, and from NCEP-DOE Reanalysis 2 (NCEP2; Kanamitsu et al., 2002). Some models biases are evident. To the east, there is a split intertropical convergence zone; this is a common problem in AOGCMs (e.g. Lin, 2007), and is also a manifestation of the Pacific equatorial cold tongue bias. The model has overly strong westerly winds in the equatorial eastern Indian ocean, overly strong ascent in the centre of the ITCZ, and weak subsidence over south-eastern Australia and part of south-east Asia. However, most of the broad features are well captured by the model. The wind vectors in both panels clearly show the Asian winter monsoon, the strong subtropical anticyclone in the southern Indian Ocean, and the monsoon shear line across northern Australia. The vertical velocity field shows ascent along the equator, and strong subsidence over Asia and the subtropics of the Southern Hemisphere.

Assessing the interannual variability in the model can provide insights into the realism of the simulated mechanisms. ENSO is a useful proxy for long-term changes in the Walker circulation associated with anthropogenic forcing, although there are differences in the underlying mechanism and associated patterns (Vecchi and Soden, 2007;

ACPD
12, 5107–5188, 2012

Lu et al., 2008). In the next three figures, we show regressions of various quantities for DJFM against SST averaged over the Niño-3.4 region (170° W–120° W, 5° S–5 N°), hereafter Niño-3.4 SST. For SST observations we use the 1° gridded analysis from HadISST 1.1 (Rayner et al., 2003).

An anticyclonic circulation off the coast of NWA in austral summer has been identified in response to El Niño in reanalyses (Wang et al., 2003, 2008), and GCM simulations using prescribed SSTs and/or mixed-layer ocean models (Lau and Nath, 2000; Taschetto et al., 2011). Either explicitly or by implication, these studies also showed that anomalies associated with La Niña were similar, but with opposite polarities. Does the ENSO-related variability in our model show similar behaviour?

Figure 6 shows 850 hPa winds for DJFM, regressed against Niño-3.4 SST, from the NCEP reanalysis and the HIST ensemble. A noticeable bias in the model is due to the Pacific equatorial cold tongue, which causes the equatorial westerly anomalies to extend too far to the west. The location and shape of the elongated anticyclonic anomaly off the coast of NWA are similar in the model and reanalysis, and also resemble the feature shown by Wang et al. (2003) (their Fig. 1c).

Figure 7 shows DJFM SST, regressed against Niño-3.4 SST, from observations and the HIST ensemble. The observations show the familiar horseshoe-shaped pattern of SST anomalies in the Pacific Ocean, as well as a warming of most of the Indian Ocean. The latter is substantially captured by the model, and is due to the "atmospheric bridge" from the Pacific Ocean (Klein et al., 1999; Alexander et al., 2002). The warming of the Indian Ocean can be mostly explained by decreases of cloudiness and wind speed during El Niño events, and vice-versa during La Niña events (Klein et al., 1999). The model shows the effect of the equatorial Pacific cold-tongue bias, with positive SST anomalies extending too far to the west. To the north-west of Australia, the region of positive SST anomalies is too small and too weak, and further south, the region of negative SST anomalies is too large and too strong. These negative anomalies can be explained by a strengthening of the Indonesian Throughflow and Leeuwin Current in La Niña years (Feng et al., 2008); these currents transport heat from the tropical Pacific warm pool,

ACPD
12, 5107–5188, 2012

southward along the coast. The positive anomalies further north reflect weaker latent cooling of the ocean surface in El Niño years, due to weaker monsoonal north-westerly winds; in La Niña years there is stronger latent cooling associated with stronger monsoonal north-westerly winds (Hendon, 2003). The distortion of these features in the model suggests that the balance of such competing processes is not accurately captured. However, to first order, the anomalous SST gradients off the coast of NWA are simulated by the model.

Figure 8 shows DJFM rainfall over Australia, regressed against Niño-3.4 SST, from observations and the HIST ensemble. The modelled ENSO-rainfall relationship in Mk3.6 (Fig. 8b) is somewhat too strong over NWA, though it also tends to be too strong over much of the continent, including parts of north-eastern Australia. There is no clear evidence of a westward bias of the ENSO-rainfall relationship over Australia, as documented for the CMIP3 multi-model ensemble mean by Cai et al. (2011b).

4.2 Simulated rainfall trends

We briefly compare rainfall trends for both June–September (JJAS) and DJFM over the wider Indo-Pacific region, to put the Australian results in a wider context. Statistical significance of ensemble means at each grid point is assessed using a two-sided *t* test, taking the 10 individual trend values as independent data points (Deser et al., 2012). For the difference of two ensemble means at each grid point (e.g. HIST minus NO_AA), a two-sample t-test for the difference of the mean of two populations is used (Zar, 1996, chapter 8).

Figure 9 shows ensemble-mean rainfall trends from GHGAS, HIST and the aerosol-induced effect (HIST minus NO_AA) over the low latitudes of the Indo-Pacific region. In JJAS, GHGAS (Fig. 9a) shows evidence of increasing monsoonal rainfall over parts of South and Southeast Asia, similar to the multi-model mean for 21st century projections in Meehl et al. (2007). Anthropogenic aerosol forcing (Fig. 9c) causes a decrease of rainfall over Southeast Asia and the tropical western Pacific. These are broadly similar to those reported recently by Bollasina et al. (2011), except that our model does not capture the observed rainfall decrease over central-northern India in HIST (Fig. 9e).

ACPD
12, 5107–5188, 2012

The aerosol-induced effect in JJAS also shows a tendency for increasing rainfall over Australia; this appears to be consistent with earlier suggestions of a southward shift of tropical rainfall in response to regional forcing from Asian aerosols (Rotstayn et al., 2007). In terms of circulation, this would be seen as a suppression of the upward branch of the local Hadley circulation north of the Equator, and a compensating weakening of subsidence to the south (Bollasina et al., 2011, their Figs. 3 and S9).

In DJFM, the main features seen in Fig. 9 are quite different. In GHGAS, the dominant feature is an increase of rainfall over the equatorial western Pacific Ocean, and a horseshoe-shaped pattern of decreasing rainfall to its west, covering parts of Southeast Asia and Australia. The aerosol-induced effect in DJFM (Fig. 9d) resembles the inverse of the GHG-induced pattern, with a strong decrease of rainfall over the equatorial western Pacific Ocean. The changes in DJFM are suggestive of an eastward (westward) shift in the upward branch of the Pacific Walker circulation in response to GHG (aerosol) forcing. Similar GHG- and aerosol-induced changes have been noted before in other models (Xie et al., 2010; Bollasina et al., 2011). Over the Indian Ocean, GHGAS shows a westward shift of equatorial rainfall from the maritime continent towards the central Indian Ocean, and the aerosol-induced effect is again of opposite sign. In Fig. 9d, an area of decreasing rainfall centred on southern Borneo is likely a result of regional aerosol-induced negative radiative forcing, which may suppress convection; this is present in the annual mean (Fig. 2) and also in DJFM (not shown).

Interestingly, there is much less evidence of a large-scale aerosol-induced southward shift of rainfall in DJFM than in JJAS. A plausible explanation is that, in JJAS, changes in the local Hadley circulation are due to changes in latent heating induced by increasing aerosols in the region of the Asian summer monsoon. However, in DJFM, there is insufficient latent heating to provoke a large-scale southward shift in the local Hadley circulation and the associated rainfall. This raises interesting questions about the mechanism by which anthropogenic aerosols affect simulated Australian rainfall trends in this season.

ACPD
12, 5107–5188, 2012

We now focus in more detail on DJFM, when there has been a significant increase of rainfall over Australia's north-west in recent decades (Fig. 1). The time history of this increase is plotted in Fig. 10, which shows an increasing trend since roughly the middle of the 20th century. The shorter (30- and 40-yr) trends are not significant, but their magnitudes are comparable to that of the 60-yr trend from 1951 to 2010. Note that there was a rainfall minimum in the early 1950s, so trends beginning in 1951 will be relatively large.

We now consider the modelled rainfall trends. Figure 11 shows ensemble-mean DJFM rainfall trends over Australia from HIST (1951–2010) and RCP4.5 (2011–2100). HIST shows modest increases over some areas, but these are mostly not significant. In contrast, RCP4.5 shows substantial, statistically significant decreases over most of the continent, and especially in the tropics.

How are the differences between the historical and projected rainfall trends in Fig. 11 to be reconciled? Figure 12 shows historical, ensemble-mean rainfall trends under different forcing assumptions, and sheds some light on this question. Rainfall trends in GHGAS are similar to those in RCP4.5, though of smaller magnitude; this is consistent with the expected dominant role of GHG forcing in RCP4.5. NO_AA is similar to GHGAS, though the negative rainfall trends are somewhat weaker. Bearing in mind that NO_AA is the same as GHGAS with the addition of natural and ozone forcing, this can be understood by reference to natural and (especially) ozone-induced changes. Rainfall trends in Fig. 12c (NAT) are weakly positive over substantial areas of Australia, though mostly not significant. Interestingly, the ozone-induced trends in Fig. 12d (HIST minus NO_OZ) are mostly positive, and are also significant over substantial areas.

The ozone-induced rainfall changes over Australia are part of a broader rainfall increase across the low latitudes of the Southern Hemisphere (not shown). This effect is similar to that obtained by Kang et al. (2011) using two models. They found that Antarctic ozone depletion causes a poleward shift of the extratropical westerly jet, which in turn induces a poleward shift of the subtropical edge of the Hadley cell. The poleward shift of this edge drives anomalous upper-level mass divergence between 15° S and

ACPD
12, 5107–5188, 2012

35° S, and this causes anomalous rising motion in the subtropics. Our model appears consistent with the result from Kang et al. (2011) regarding the importance of ozone changes for understanding recent summer rainfall trends in the Southern Hemisphere. One caveat is that NO_OZ suppresses changes in both stratospheric and tropospheric ozone, so in principle our simulations are not designed to distinguish between these effects. In view of this, and the fact that our main focus is to contrast the effects of changes in aerosols and long-lived GHGs, we will not further analyse the effects of ozone changes,

The aerosol-induced rainfall changes in Fig. 12e (HIST minus NO_AA) indicate that, in CSIRO-Mk3.6, aerosol forcing has countered the effects of a GHG-induced decrease of Australian summer rainfall. The mechanisms will be investigated in Sect. 4.3. Figure 12f (ASIA minus NO_AA) isolates the effects of changes in Asian aerosols; it is seen that the effects are similar to those of all anthropogenic aerosols, though the rainfall trends are somewhat weaker, and there is less statistical significance. This suggests that the rainfall changes in Fig. 12e are substantially, but not entirely, due to Asian aerosols, which is broadly consistent with the results of low-resolution modelling by Rotstayn et al. (2007). One interpretation is that, based on this low-resolution model, non-Asian aerosols make an important contribution to the suppression of the Asian monsoon (Cowan and Cai, 2011), so it is still possible that the effect is mediated mostly or entirely through changes in the Asian monsoon.

Figure 13 compares observed and modelled trends in rainfall, averaged over the same area of NWA as used in Fig. 10. Individual 1951–2010 trends from the 10-member forced ensembles, and 440 unforced 60-yr trends from the 500-yr preindustrial control run (piControl), are shown as small black dots. (These were calculated using a moving 60-yr window over the 500-yr run.) The observed 60-yr trend (shown as a red line) is not reproduced by any of the 440 unforced trends. This suggests that there is a forced component in the observed trend, or that decadal variability is underestimated by the model. There is no evidence that interannual variability is underestimated by the model; in fact, the standard deviation of the 499 individual DJFM rainfall values in

ACPD
12, 5107–5188, 2012

piControl is 1.31 mm per day, larger than the observed value of 0.75 mm per day for the detrended time series. 95 % confidence intervals for GHGAS and HIST minus NO_AA confirm that the ensemble-mean GHG- and aerosol-induced rainfall trends are significantly different from zero, and of opposite signs. For HIST minus NO_AA, even though we did not assume that the individual runs are paired when testing for significance, we have plotted individual trend values by pairing run 1 from HIST with run 1 from NO_AA, and so on. (The runs that were paired in this way do share a common branch time from the pre-industrial control run.) Two of the individual "HIST minus NO_AA" trends are larger than the observed trend value.

The fact that HIST minus NO_AA is able to capture the magnitude of the observed trend in some of its ensemble members suggests that anthropogenic aerosol forcing combined with natural variability may be sufficient to explain the observed rainfall increase over NWA. However, it must be noted that the model does not simulate the observed rainfall increase in response to "all forcings" (HIST), even in a single ensemble member. Further, as mentioned in the Introduction, the rainfall response in this region is likely to be model-dependent. Bearing these caveats in mind, we investigate the mechanisms of the simulated and observed rainfall trends over NWA in the remainder of this section.

4.3 Simulated and analysed changes in circulation

What is the mechanism by which changes in long-lived GHGs and aerosols exert effects of opposite sign on Australian summer rainfall in CSIRO-Mk3.6? We address this question by investigating the changes in circulation associated with each forcing agent.

Changes in tropical circulation are often driven by SST anomalies relative to the surrounding ocean (Xie et al., 2010; Watterson, 2010). An important underlying mechanism is the generation of lower-tropospheric pressure gradients, which induce moisture convergence (Lindzen and Nigam, 1987). Thus we compare trends in T_s, after subtraction of the mean low-latitude (30° S to 30° N) trend from each ensemble (hereafter referred to as T_{rel}). Figure 14 shows that T_{rel} trends in GHGAS qualitatively share many features with the strong GHG-driven pattern in RCP4.5: there is enhanced warming

ACPD
12, 5107–5188, 2012

over continental areas, a result typical of the response of GCMs to increasing GHGs (Meehl et al., 2007) and also in the western and central equatorial Pacific (Liu et al., 2005b; DiNezio et al., 2009), though the latter feature is more extended to the east in RCP4.5. There is relatively less warming in the Southern Hemisphere than in the Northern Hemisphere, consistent with the multi-model mean in Meehl et al. (2007), and also in the eastern tropical Indian Ocean (Xie et al., 2010). More rapid warming in the Northern Hemisphere is a robust feature of transient simulated climate change; it is related to the larger proportion of land in the Northern Hemisphere, and more efficient downward transport of heat by the oceans of the Southern Hemisphere (Boer et al., 2000).

T_{rel} trends in HIST (Fig. 14c) are much weaker than those in GHGAS and RCP4.5, and the features identified above are absent or much reduced. The aerosol-induced effect in Fig. 14d highlights that this is largely due to the inclusion of aerosol forcing in HIST. Several features of Fig. 14d are of opposite sign to those in Figs. 14a and 14b: over South and East Asia there is relative cooling, due to negative forcing by anthropogenic aerosols. In contrast, relative cooling over Australia is caused by increasing rainfall there (Fig. 12e). In the western equatorial Pacific, there is relative cooling instead of enhanced warming. In the Southern Hemisphere, the pattern is also very different, with relative warming over much of the Pacific Ocean, and in the tropical eastern Indian Ocean.

Figure 15 shows trends of velocity potential and divergent wind vectors at 200 hPa; with the sign convention used here, cool (warm) colours denote centers of increasing (decreasing) upper-level divergence and ascending motion. RCP4.5 shows increasing upper-level divergence over the tropical central-western Pacific, and decreasing upper-level divergence over the maritime continent. The pattern in GHGAS resembles a slightly weaker version of the strong GHG-forced trend seen in RCP4.5, and the trend pattern in HIST is weaker again. The aerosol-induced effect (Fig. 15d) has the opposite polarity, and suggests that the weaker trend pattern in HIST compared to GHGAS is due to the offsetting effect of aerosol forcing.

ACPD
12, 5107–5188, 2012

Another view of the circulation changes induced by changes in long-lived GHGs and anthropogenic aerosols is given by trends in 850 hPa wind vectors and 500 hPa vertical velocity (Fig. 16). The wind trends show that in GHGAS, there is weaker convergence of zonal winds over the Indonesian region, consistent with a weakening Walker circulation, whereas the reverse is true for the aerosol-induced effect in panel b. The changes in equatorial zonal winds in both ocean basins are driven by an increasing pressure gradient towards the Indonesian region in GHGAS, and vice versa in HIST minus NO_AA (not shown); this is similar to the findings of Vecchi and Soden (2007) and Bollasina et al. (2011).

The horseshoe-shaped vertical-velocity trend patterns in Fig. 16 are broadly consistent with the DJFM rainfall trends in Fig. 9. They also confirm the eastward (westward) shift of the main equatorial convection centre in response to GHG (aerosol) forcing. After allowing for the equatorial Pacific cold tongue bias, which causes the equatorial Pacific anomalies to extend too far west towards Indonesia, the pattern in GHGAS (HIST minus NO_AA) resembles an El Niño-like (La Niña-like) anomaly pattern for austral summer (e.g. Wang et al., 2003, their Fig. 1c). This includes the trends over northern Australia and the southern Indian Ocean, and the anticyclonic (cyclonic) circulation trend pattern off the coast of NWA, which we showed in Fig. 6; we shall return to these regional aspects below.

The eastward shift of the main equatorial convection centre in response to GHG forcing (Figs. 15 and 16) is similar to that shown previously for an ensemble of CMIP3 GCMs forced by increasing GHGs (Vecchi and Soden, 2007). They related these changes to a weakening of the tropical circulation (and especially the Walker circulation), consistent with an increase in lower-tropospheric water vapour in a warmer climate (Held and Soden, 2006; Zhang and Song, 2006).

Vecchi and Soden (2007) also showed that the simulated changes in the tropical Pacific have an "El Niño-like" character, but the mechanisms are distinct from those of El Niño. In particular, the weakening of the Pacific Walker circulation (quantified as a change in the zonal sea-level pressure gradient) was reproduced in atmospheric

ACPD
12, 5107–5188, 2012

GCMs with mixed-layer oceans; this indicates that the driving mechanism is atmospheric, whereas El Niño is a coupled ocean-atmosphere phenomenon. In our model, a strong eastward shift of the main convection centre is also reproduced in a doubled-CO_2 experiment with a mixed-layer ocean (not shown), with the difference that the eastward pole is centred at approximately 150° W, instead of near 165° E as in RCP4.5 (Fig. 15a).

The modelled GHG-induced changes in equatorial SSTs can be substantially understood in terms of changes in the Walker circulation (Vecchi and Soden, 2007; DiNezio et al., 2009; Xie et al., 2010). A weaker Walker circulation gives weaker convergence of near-surface zonal winds over the Indonesian region. Over the eastern Indian Ocean, anomalous equatorial easterlies occur, with an increase in upwelling and a shallowing thermocline. This contributes to the relative cooling off the coasts of Java and Sumatra in Figs. 14a and 14b. This feature is strong in austral winter and spring, when the climatological southeasterly winds that flow along the coastlines of Sumatra and Java induce upwelling and a shallow thermocline and permit an air-sea positive feedback process known as Bjerknes feedback (Saji et al., 1999; Schott et al., 2009). The SST anomaly then decays during austral summer.

The enhanced Pacific equatorial warming due to increasing GHGs in 11 AOGCMs was studied in detail by DiNezio et al. (2009). Enhanced warming along the equator was mainly due to changes in zonal and meridional oceanic heat advection, driven by a slowing down of the Pacific Walker circulation. They also found that ocean dynamical changes act to reduce the net heating in the east, and enhance it in the west. This explains why models simulate enhanced equatorial warming, rather than El-Niño-like warming, in response to a weaker Walker circulation. It also explains why, in our coupled AOGCM, equatorial convection increases near the location of maximum SST increase around 165° E in RCP4.5 (and to a lesser extent in GHGAS), instead of near 150° W as it does when a mixed-layer ocean is used.

We now return to Fig. 16, which shows some notable changes in circulation in the Australian region. In particular, off the coast of NWA, there is an anticyclonic (cyclonic)

ACPD
12, 5107–5188, 2012

circulation trend in GHGAS (HIST minus NO_AA). An effect of this circulation trend is to weaken the monsoonal flow across the north coast of Australia in GHGAS, and strengthen it in HIST minus NO_AA. Trends in RCP4.5 (not shown) show similar patterns to those in GHGAS, but are of larger magnitude.

The centres of the circulation trends off the coast of NWA are also very close to the centres of the regression patterns shown in Fig. 6. In particular, the tropical regression pattern in Fig. 6b closely resembles the trend pattern in GHGAS (Fig. 16a), which suggests that the mechanism underlying the GHG-forced circulation changes in the tropics may be similar to that in ENSO. However, note that the patterns in the midlatitudes (e.g. over southern Australia) are very different, reflecting a broadening of the Hadley circulation in response to forcing from long-lived GHGs, and a narrowing during El Niño (Lu et al., 2008).

It is noticeable that the trends in vertical velocity (ω) at 500 hPa are offset from the centres of the circulation trends in Fig. 16, in common with the results of Wang et al. (2003), who analysed interannual variations associated with ENSO. This can be explained in terms of Sverdrup vorticity balance (e.g. Rodwell and Hoskins, 2001),

$$\beta v \approx f \frac{\partial \omega}{\partial p}, \tag{2}$$

which expresses conservation of absolute vorticity. Here, v is meridional wind, p is pressure, f is the Coriolis parameter, and β is its meridional gradient. Equation (2) implies that poleward motion is associated with ascent in the mid-troposphere ("stretching" of the air column), whereas equatorward motion is associated with subsidence. This agrees well with the vertical velocity trends of opposite sign to the north-east and south-west of the horizontal circulation features centred off the coast of NWA in Fig. 16.

We also calculated trends of moisture transport ($q\boldsymbol{V}$) and moisture convergence $-\nabla\cdot(q\boldsymbol{V})$, and vertically integrated these through the depth of the atmosphere for GHGAS and HIST minus NO_AA (Fig. 17). The calculation is based on six-hourly instantaneous fields of specific humidity (q) and horizontal winds ($\boldsymbol{V}$). Associated with the circulation trends shown in Fig. 16, there is a decreasing trend of moisture convergence over NWA

ACPD
12, 5107–5188, 2012

in GHGAS, and an increasing trend in HIST minus NO_AA. The streamlines suggest that in HIST minus NO_AA, the source of increasing moisture for NWA comes from both the equatorial western Pacific and south of the equator in the central Indian Ocean; both of these areas show a decreasing rainfall trend (Fig. 9d) and a trend of increasing subsidence (Fig. 16b). The converse applies in GHGAS.

Is there evidence for a cyclonic circulation trend off the coast of NWA in reanalyses? We use data from the ERA-Interim Reanalysis (Dee et al., 2011), NCEP/NCAR Reanalysis 1 (NCEP1; Kalnay et al., 1996) and NCEP-DOE Reanalysis 2 (NCEP2; Kanamitsu et al., 2002). Of these, only NCEP1 provides data prior to the advent of satellite retrievals in 1979. However, various discrepancies have been noted in NCEP1, especially prior to the late 1970s (e.g. Wu et al., 2005), so we calculate trends from NCEP1 both for the full 60-yr analysis period (1951–2010) and for 1980–2010 (i.e. December 1979 to March 2010).

Figure 18 shows trends in DJFM horizontal winds at 850 hPa and vertical velocity at 500 hPa from each reanalysis. All the analysed trends for 1980–2010 show a cyclonic circulation anomaly off the coast of NWA, and a similar feature is also evident in the 1951–2010 trend from NCEP1. The cyclonic trend anomaly for 1951–2010 is offset slightly to the north-east, relative to the trends shown for 1980–2010. With the exception of ERA-Interim, the cyclonic trend anomaly in each case is associated with anomalous ascent (subsidence) to the north and east (south and west) of the circulation centre, as in the model. Although there are many differences in the details, all the plots also show easterly wind trends in equatorial winds over the western Pacific Ocean, and westerly wind trends over the eastern Indian Ocean, suggesting a strengthening of the Walker circulation over the time period. A trend of increasing equatorial westerly winds over the Indian Ocean during 1961–2000 in data from the ECMWF 40 Year Reanalysis (ERA 40) was noted by Trenary and Han (2008) and Han et al. (2010). However, Tokinaga et al. (2012) found evidence for a weakening trend during 1950–2008, using bias-corrected ship-based observations, so this is uncertain. Another aspect of Fig. 18 is that the trend magnitudes in the reanalyses are generally

ACPD
12, 5107–5188, 2012

larger than those in Fig. 16, reflecting the fact that the modelled trends are averaged over 10 ensemble members.

4.4 What is the cause of the circulation trends?

How do anthropogenic aerosols induce a cyclonic circulation trend off the coast of NWA in the model? The mechanism could involve changes in the local Hadley circulation or the Walker circulation. Either of these effects could be primarily atmospheric or involve oceanic changes. The latter could include air-sea interactions or changes in oceanic heat transports (which in turn affect SSTs). We propose an atmospheric mechanism that involves a Rossby wave response to convective heating anomalies, and also discuss the possible role of air-sea interactions. Bearing in mind that the system includes multiple feedbacks, the following discussion does not attempt to be exhaustive.

We argue that there is a Rossby wave response to off-equatorial convective heating anomalies in the transition to austral summer, which is enhanced by a positive feedback process that causes the cyclonic anomaly to grow strongly during DJFM. The Rossby wave response to an off-equatorial positive heating anomaly is slightly different from the classic Gill-Matsuno response to a heating anomaly centred on the equator (Matsuno, 1966; Gill, 1980). Rather than twin cyclones that straddle the equator to the west of the heat source, the expected lower-tropospheric response to a tropical heat source south of the equator is a cyclonic anomaly located to its south-west (e.g. Moura and Shukla, 1981; Wang et al., 2000).

In the proposed mechanism, the effect of anthropogenic aerosols is mediated via the local Hadley circulation. Recall that in boreal summer (JJAS), our simulations show an aerosol-induced southward shift of equatorial rainfall between roughly 50° E and 150° E (Fig. 9c). As we discussed, the large-scale aerosol-induced response of our model in DJFM more closely resembles a zonal shift associated with a change in the Walker circulation. However, closer examination shows that a coherent southward shift of tropical circulation and rainfall persists until late in the calendar year.

ACPD
12, 5107–5188, 2012

Here we show how the simulated aerosol-induced effects on the local Hadley circulation change between boreal summer and austral summer. Figure 19 shows trends in vertical pressure velocity (shaded) from HIST minus NO_AA, zonally averaged between 70° E and 130° E. In July (Fig. 19a), the response resembles that shown by Bollasina et al. (2011) (their Figs. 3 and S9), namely, a weakening of upward motion associated with the Asian summer monsoon, and enhanced upward motion centred south of the Equator. The pattern can be described as a broad southward shift of the upward branch of the local Hadley circulation. The maximum aerosol-induced change (~25 hPa per day per 100 yr) is substantial relative to the mean upward motion (maximum ~60 hPa per day). By September (Fig. 19b), the area of weakening upward motion is narrower, and centred further south (near 5° N). There are areas of compensating, enhanced upward motion to the south and north. The marked change between July and September may be related to the southward shift of the latitude of maximum insolation. In November (Fig. 19c), the pattern resembles that in September with a slight southward shift, and some weakening of the trends is also seen. By January (Fig. 19d), consistent with our results for DJFM, aerosol-induced effects on the local Hadley circulation are barely evident.

Figure 20 shows trends in rainfall and 850 hPa winds from HIST minus NO_AA, for November, December, February and March. November coincides with the transition between summer and winter monsoonal winds over the Indian Ocean (e.g. Hastenrath and Polzin, 2004). In that month, (Fig. 20a) Mk3.6 shows a clear southward shift of equatorial rainfall south of the Asian continent, consistent with the circulation changes shown in Fig. 19c. Note that the pattern over the Indian Ocean also resembles a negative Indian Ocean Dipole event, with positive rainfall anomalies off the coast of Sumatra, and negative anomalies south and south-west of India. (This is consistent with the expected response to westerly equatorial wind anomalies off Sumatra during austral winter and spring, as discussed above.) There is a cyclonic circulation anomaly in the south-eastern Indian Ocean, and its location is roughly consistent with a Rossby wave response to the positive heating anomaly near Java. In December, there is still

ACPD
12, 5107–5188, 2012

some remaining evidence of a southward shift of equatorial rainfall. The cyclonic circulation is less coherent in December than in November; it has split into two smaller cells, which appear to correspond to the positive convective heating anomalies centred near Sumatra and off the north coast of Australia. In January (not shown), the cyclonic circulation feature becomes stronger and re-forms as a single, elongated cell. It is stronger again in February, and is centred just off the coast of NWA. It's location appears consistent with the peak convective heating trend over northern Australia, and its elongated shape can also be explained by the extended band of increased convective heating that extends in a westerly direction from the top end of Australia.

Interestingly, in March, which generally corresponds to the retreat of the Australian monsoon (e.g. Kajikawa et al., 2010), the aerosol-induced effect appears as an even stronger enhancement of the monsoonal north-westerly winds compared to February, and the enhanced north-westerlies extend even further westward towards the central Indian Ocean. This suggests that the process we have described entails a positive feedback, in which moisture convergence (Fig. 17) due to a stronger cyclonic circulation enhances the monsoonal convective heat source, which in turn enhances the circulation via the Rossby wave response. We note that Kajikawa et al. (2010) referred, in passing, to the cyclonic circulation anomaly associated with the Australian monsoon as a Rossby wave response to the latent heating released in the monsoonal rainfall.

Do SSTs have a substantial role in forcing the circulation trends off the coast of NWA in the model? It is noticeable that the south-eastern tropical Indian Ocean is an area where T_{rel} increases (decreases) quite strongly in HIST minus NO_AA (GHGAS) in Fig. 14. It is possible that changes in the Indonesian Throughflow (ITF) contribute to these trends. The ITF is recognised as an important heat source for the south-eastern Indian Ocean (Hirst and Godfrey, 1993; Schneider, 1998), and it tends to weaken in response to weaker easterly winds in the equatorial western Pacific (Meyers, 1996; Alory et al., 2007). Simulated changes in the ITF transport during 1951–2010 show an increase in HIST minus NO_AA and a decrease in GHGAS, so they are in the right

ACPD
12, 5107–5188, 2012

sense to contribute to the T_{rel} trends. However, the changes (not shown) were of the order of 10 %, and it is unclear whether they would have a substantial effect. A rigorous assessment would require a detailed analysis of the oceanic heat budget, which we intend to address in a separate study.

It is interesting that T_{rel} trends in GHGAS and HIST minus NO_AA have maximum magnitudes near 20° S, 110° E, nearly colocated with the circulation centres (Fig. 14b and d). The locations of the cyclonic or anticyclonic circulation centres were similar in analysed trends (Fig. 18) and ENSO-related inter-annual variations (Fig. 6). Here we show that the T_{rel} maxima likely represents a positive air-sea feedback, which may help to "anchor" the circulation anomaly in a preferred location off the coast of NWA in austral summer.

Figure 21 shows DJFM trends in 10-m wind speed from GHGAS and HIST minus NO_AA. Vectors in panel a represent the *mean* climatological 10-m winds for DJFM, whereas vectors in panel b show the *trends* in 10-m winds in HIST minus NO_AA. The mean trade winds (Fig. 21a) are almost southerly along the coast, and further north they turn eastward to form the north-westerly monsoon. A cyclonic wind trend pattern off NWA in HIST minus NO_AA (Fig. 21b) increases surface wind speed on all sides of the cyclone centre, by enhancing monsoonal northwesterly winds to the north and east, and the trade winds to the south and west. Thus SSTs (in relative terms) will tend to be reduced around the centre of the cyclone by increased latent cooling and ocean vertical mixing, reducing the tendency of convection and the associated cyclonic anomaly to move in any direction. Note that the surface cyclonic anomaly is located slightly to the west of the 850 hPa feature shown in Fig. 16b, so northerly flow on its eastern flank creates the area of decreasing wind speed off the coast of NWA in Fig. 21b. The westward offset of the near-surface cyclonic feature is consistent with a Rossby wave response to the local heating anomaly.

The converse of the above argument applies for an anticyclonic trend pattern in GHGAS (Fig. 21a), which causes increasing wind speed to the north, west and south. Note that the wind speed trends off the coast of NWA in GHGAS are almost the inverse

ACPD
12, 5107–5188, 2012

of the pattern in HIST minus NO_AA, though there are differences in the detail.

Comparison of Fig. 21b with Fig. 14d suggests that the local maximum in the T_{rel} trend off the coast of NWA in HIST minus NO_AA arises, at least in part, due to the effect of the atmosphere on the ocean. On the other hand, positive SST anomalies in the tropics tend to induce convection, with moisture convergence likely to be more important than enhanced surface evaporation (Lindzen and Nigam, 1987; Moura and Shukla, 1981). Thus it is also plausible that the local T_{rel} trend maximum induces convection and a cyclonic circulation anomaly, suggesting that a positive air-sea feedback is at work.

There are precedents for this idea in the ENSO literature. The importance of air-sea interactions for the rapid growth of the south-eastern Indian Ocean anticyclone during the austral spring of a developing El Niño was emphasised by Wang et al. (2003). Similarly, air-sea interactions are considered to be important for the amplification and maintenance of the anomalous anticyclone in the western North Pacific during El Niño events (Wang et al., 2003; Wu et al., 2010).

Do SST observations shed any light on this matter? Two globally complete, historical SST analyses are the 1° HadISST 1.1 data set and the 2° NOAA Extended Reconstructed Sea Surface Temperature analysis (ERSST.v3b). ERSST.v3b is as described by Smith et al. (2008), except that satellite SST retrievals are not used in ERSST.v3b. HadISST and ERSST.v3b use different statistical procedures to smooth the data and fill in missing values; a further difference between them is that HadISST includes information from satellite retrievals.

Figure 22 shows SST trends (relative to the low-latitude mean trend) from HadISST and ERSST.v3b for 1951–2010. There is less agreement over the south-eastern Indian Ocean than over much of the Pacific Ocean. There is an area along the NWA coastline where both data sets show a negative SST trend, which could be consistent with increasing monsoonal north-westerlies. As noted by Deser et al. (2010) accurate calculation of SST trends is hampered by sparse sampling and inhomogeneous measurement practices. Further, the tropical south-eastern Indian Ocean is a relatively

ACPD
12, 5107–5188, 2012

data-sparse region; see the SST coverage maps at http://icoads.noaa.gov/r2.5sst.html, which extend Fig. 3 of Woodruff et al. (2011) to a range of different time periods. Thus the analysed SST trends in this region are not sufficiently robust to resolve the relatively modest SST gradients seen off the coast of NWA in the model.

4.5 Further discussion

Our results suggest that a lower-tropospheric cyclonic circulation trend off the coast of NWA is the key process that underlies the NWA rainfall increase. The trend pattern, in both HIST minus NO_AA and reanalyses, resembles the pattern associated with ENSO-related variability, and yet changes in ENSO do not explain the trend in NWA rainfall. Further, the trend in NWA rainfall has persisted, despite fluctuations in the Inter-decadal Pacific Oscillation (IPO; Power et al., 1999; Parker et al., 2007). (The IPO bears some similarity to the Pacific Decadal Oscillation, which is defined over the North Pacific, whereas the IPO is a wider Pacific basin phenomenon. It can be seen loosely as a "slow" version of ENSO.) This raises intriguing questions about the cause of the cyclonic circulation trend. Our results suggest that anthropogenic aerosol forcing makes an important contribution to this trend, though the balance between the compensating effects of long-lived GHGs and aerosols in our runs is an unresolved issue.

In the mechanism we propose, the aerosol-induced cyclonic circulation trend off the coast of NWA in DJFM is triggered by a southward shift of the local Hadley circulation late in the calendar year (November–December), whereas by January this southward shift has all but disappeared in our simulations. However, in the zonal mean, the DJFM Hadley circulation does shift southward in HIST minus NO_AA (not shown). An interesting related issue is that reanalyses suggest that, in the zonal mean, the austral summer Hadley circulation has become stronger during the last few decades, though there are questions about the robustness of this finding (Mitas and Clement, 2005; Song and Zhang, 2007). These are interesting topics for further research.

ACPD
12, 5107–5188, 2012

A cyclonic circulation anomaly off the coast of NWA was also identified by Shi et al. (2008) and Lin and Li (2012) in studies of the NWA rainfall trend. Shi et al. (2008) used empirical orthogonal functions to determine two modes of interannual variability of Australian summer rainfall. The first of these modes was associated with a cyclonic circulation anomaly off the coast of NWA, and they argued that variations of this mode were instigated by a pattern of enhanced SST gradients toward the Australian coast in the Indian Ocean. However, as shown in Fig. 22, observed SSTs do not show evidence of such a trend, so this remains an open question. Further, our simulations suggest that the SST trend pattern in this region is likely to be at least partly due to the effect of the atmosphere on the ocean, so the role of SSTs as a driver is uncertain. Lin and Li (2012) linked the observed NWA rainfall increase (and associated circulation anomalies) to a Rossby wave train that travels eastward from the tropical Atlantic Ocean, embedded in the westerly jet waveguide of the Southern Hemisphere. They thus suggested that the observed rainfall increase in NWA may be driven, at least in part, by enhanced ascent induced by increasing SST in the tropical Atlantic. This is an interesting hypothesis that merits further research.

An important way forward will be to compare the responses of other CMIP5 models; it is hoped that this will include a substantial set of runs that isolate the anthropogenic aerosol forcing (Boucher et al., 2011). The NWA rainfall response to increasing GHGs (and presumably anthropogenic aerosols) is model-dependent (Watterson, 2012; Cai et al., 2011b). This might reflect the fact that NWA is on the fringe of a region with very heavy rainfall, so it's response under climate change is likely to be a delicate balance between competing dynamic and thermodynamic effects (Chou and Neelin, 2004; Held and Soden, 2006). Exploring the phase space of possibilities in two dimensions (forcing and models) is likely to yield more insights than can be gained from a single model.

CSIRO-Mk3.6 projects strongly decreasing rainfall over much of Australia in the 21st century (in the annual mean as well as DJFM), which is an alarming result for a country that has limited water resources. Watterson (2012) compared 21st century simulations from 23 CMIP3 GCMs and found that projected Australian rainfall changes correlated

ACPD
12, 5107–5188, 2012

strongly with changes in a "Pacific-Indian Dipole index", similar to the equatorial SST trend pattern seen in our runs dominated by GHG forcing; in other words, models that project a relatively warm central-western Pacific and a relatively cool eastern Indian Ocean tend to project a stronger decrease of rainfall over Australia, including NWA. A majority of models project a decrease of rainfall over NWA, but a sizeable minority project an increase. Based on this categorisation, the predecessor of CSIRO-Mk3.6 (Mk3.5) was among the models with the largest projected rainfall decreases, and Mk3.6 behaves similarly. Further, Cai et al. (2011a) showed that GCMs with stronger Indian Ocean Dipole (IOD) variability tend to produce a slower eastern Indian Ocean warming rate and greater future rainfall changes in IOD-affected regions, including Australia. Using the method from Cai et al. (2011a), Mk3.6 has an IOD amplitude of 0.40 °C, more than twice the observed value. These results provide some insight into why our model simulates a relatively strong drying trend over Australia in RCP4.5.

5 Summary and conclusions

We described a version of the CSIRO GCM (CSIRO-Mk3.6), which includes a prognostic aerosol scheme and treatments of direct and indirect aerosol effects. The total anthropogenic aerosol forcing in the model was estimated as $-1.4\,\mathrm{W\,m^{-2}}$ between 1850 and 2000. This is a little larger in magnitude than the best estimate of $-1.2\,\mathrm{W\,m^{-2}}$ from Forster et al. (2007), though it is well within the large uncertainty range.

As a part of CMIP5, we used CSIRO-Mk3.6 to perform 10-member ensembles of AOGCM historical (1850–2010) simulations driven by different combinations of forcing agents, and compared these with 21st century projections based on RCP4.5. We looked at changes in rainfall and circulation in the Indo-Pacific region in DJFM, with a primary focus on the observed rainfall increase over north-western Australia (NWA) during 1951–2010, and whether this increase can be partly attributed to changes in anthropogenic aerosols. We paid particular attention to an historical ensemble forced solely by increasing long-lived GHGs (GHGAS), and aerosol-induced effects diagnosed as the difference of HIST minus NO_AA, where HIST was an ensemble with

ACPD
12, 5107–5188, 2012

"all forcings", and NO_AA was the same as HIST, except that anthropogenic aerosol forcing was suppressed.

There was a statistically significant increase (decrease) of summer rainfall over north-western and central Australia during 1951–2010 in HIST minus NO_AA (GHGAS), whereas HIST gave relatively small and insignificant rainfall changes. RCP4.5 gave a rainfall decrease with a similar pattern to that in GHGAS, but it was larger in magnitude, reflecting the stronger long-lived GHG forcing in the 21st century. Comparison of these experiments explained why the strong projected rainfall decrease in RCP4.5 was not obtained in HIST: the GHG-induced rainfall decrease was "masked" by changes in anthropogenic aerosols, and (to a lesser extent) ozone.

The model was unable to capture the large magnitude of the observed 1951–2010 rainfall increase over NWA, either in the ensemble mean of HIST minus NO_AA, or in a series of 440 unforced 60-yr trends from the pre-industrial control run. However, when we paired the individual runs from HIST with their corresponding runs from NO_AA, two of 10 realisations of HIST minus NO_AA produced 1951–2010 NWA rainfall trends that were larger than the observed value of 2.72 mm per day per century. This suggests that the observed rainfall increase includes both a forced and an unforced component, though another interpretation is that the model underestimates the decadal variability of NWA rainfall.

The aerosol-induced circulation response over the Indo-Pacific region in DJFM resembled a westward shift and strengthening of the upward branch of the Walker circulation. To first order, this is a La Niña-like response, consistent with the postulated thermodynamic effect of anthropogenic aerosols (Held and Soden, 2006; Ming and Ramaswamy, 2011; Bollasina et al., 2011). This was quite different from the response in boreal summer, when our model gave a southward shift of equatorial rainfall, consistent with the idea that anthropogenic aerosols have suppressed Asian monsoonal rainfall, and caused a southward shift of the local Hadley circulation. We attributed the different behaviour to the fact that there is insufficient latent heating across southern Asia to provoke a substantial change in the local Hadley circulation in DJFM. However, this

ACPD
12, 5107–5188, 2012

raised intriguing questions about the nature of the mechanism, because in DJFM we did not find a coherent aerosol-induced change in meridional circulation in the region between Asia and Australia, as hypothesised by Rotstayn et al. (2007).

A fundamental aspect of the mechanism in the model was a cyclonic low-level circulation trend centred off the coast of NWA in HIST minus NO_AA, and a similar response of the opposite sign in GHGAS. The aerosol-induced cyclonic trend induced moisture convergence and upward motion over NWA. Circulation trends from reanalyses showed cyclonic circulation trends off the coast of NWA with a marked similarity to the aerosol-induced trend in the model, providing evidence that the mechanism of simulated rainfall changes is realistic. Also, several studies of ENSO-related variability have identified a similar anticyclonic (cyclonic) circulation feature in response to El Niño (La Niña), in both reanalyses and models (Lau and Nath, 2000; Wang et al., 2003, 2008; Taschetto et al., 2011). To the extent that ENSO can be used as a proxy for longer-term forced trends, these studies also provide evidence that the mechanism in the model is realistic.

We showed evidence that the cyclonic circulation trend in HIST minus NO_AA was initiated as a Rossby wave response to positive convective heating anomalies south of the equator in late austral spring. In November, the aerosol-induced response of the model over the Indian Ocean still resembled that in boreal summer (namely, a southward shift of equatorial rainfall and the local Hadley circulation), whereas by January this southward shift had all but disappeared. The aerosol-induced enhancement of the cyclonic circulation off the NWA coast and the associated monsoonal rainfall became progressively stronger from December to March, suggesting that there was a positive feedback between the source of latent heat (the Australian monsoon) and the cyclonic circulation: moisture convergence due to a stronger cyclonic circulation enhanced the monsoonal convective heat source, which in turn enhanced the circulation via the Rossby wave response. If this hypothesis is correct, a relatively small initial perturbation could lead to a substantial change in NWA rainfall. We also found evidence of a positive air-sea feedback off the coast of NWA in the model, which may help to

ACPD
12, 5107–5188, 2012

"anchor" the circulation anomaly in that location in DJFM. Further work is needed to establish the veracity of these mechanisms, both in the model and in observations.

There are other caveats regarding our results. Possibly the most substantial is the large uncertainty in the magnitude and spatial pattern of anthropogenic aerosol forcing. Mk3.6 has a lower oceanic heat uptake over recent decades than observations; this may indicate that our anthropogenic aerosol forcing of $-1.4\,\mathrm{W\,m^{-2}}$ is too large in magnitude (J. Church, personal communication, 2011). Also, our model does not simulate a significant increase of NWA rainfall in the ensemble mean with "all forcings" (HIST), due to compensating effects between long-lived GHGs and aerosols; this could imply that the balance of these compensating effects is not captured accurately by the model, or that there is a large unforced component in the observed rainfall trend. Further, as discussed above, the response of NWA rainfall to increasing GHGs differs among GCMs, and a substantial minority projects a decrease instead of an increase. By implication, even if the magnitude and spatial pattern of aerosol forcing were known perfectly, the response of NWA rainfall would also differ among models. An interesting question is whether forcing due to anthropogenic aerosols and increasing GHGs in the CMIP5 models generally have opposing effects on NWA rainfall, or whether even this is model-dependent.

Subject to these uncertainties, CSIRO-Mk3.6 suggests that anthropogenic aerosols have contributed to the observed increase of NWA rainfall over the last few decades. Another implication of our results is that anthropogenic aerosols may have masked greenhouse gas-induced changes in rainfall over NWA and in circulation over the wider Indo-Pacific region: simulated trends in RCP4.5 resemble a stronger version of those in GHGAS, and are very different from those in HIST.

More generally, we argue that GCM simulations driven by individual forcing agents, or combinations thereof, are a valuable tool that can help to reduce uncertainty in future climate projections. Our results are limited by the fact that they rely on only one model. Having access to ensembles of such runs that use a range of GCMs, preferably within the CMIP5 framework, would potentially be very powerful.

ACPD
12, 5107–5188, 2012

Acknowledgements. The authors thank Alena Chrastansky for her careful reading of the manuscript, Ming Feng and Catia Domingues for helpful discussions, and Arnold Sullivan for assistance with calculation of the IOD amplitude. The Queensland Government Department of Environment and Resource Management provided the high performance computing facilities for the CSIRO-Mk3.6 simulations. The National Computational Infrastructure National Facility in Canberra provided storage and processing resources for the post-processing, and hardware for hosting the Mk3.6 CMIP5 data via the Earth System Grid. NCEP Reanalysis data were provided by the NOAA/OAR/ESRL PSD, Boulder, Colorado, USA, from their web site at http://www.esrl.noaa.gov/psd/. ECMWF ERA-Interim data used in this study were obtained from the ECMWF data server. This work was partly supported by the Australian Climate Change Science Program and the Indian Ocean Climate Initiative.

References

Ackerley, D., Booth, B. B. B., Knight, S. H. E., Highwood, E. J., Frame, D. J., Allen, M. R., and Rowell, D. P.: Sensitivity of 20th Century Sahel Rainfall to Sulfate Aerosol and CO_2 Forcing, J. Climate, 24, 4999–5014, doi:10.1175/JCLI-D-11-00019.1, 2011. 5111

Alexander, M. A., Bladé, I., Newman, M., Lanzante, J. R., Lau, N. C., and Scott, J. D.: The atmospheric bridge: The influence of ENSO teleconnections on air-sea interaction over the global oceans, J. Climate, 15, 2205–2231, 2002. 5128

Alory, G., Wijffels, S., and Meyers, G.: Observed temperature trends in the Indian Ocean over 1960–1999 and associated mechanisms, Geophys. Res. Lett., 34, L02606, doi:10.1029/2006GL028044, 2007. 5141

Arblaster, J. M. and Meehl, G. A.: Contributions of External Forcings to Southern Annular Mode Trends, J. Climate, 19, 2896–2905, 2006. 5111

Berry, G., Reeder, M. J., and Jakob, C.: Physical mechanisms regulating summertime rainfall over north-western Australia, J. Climate, 24, 3705–3717, 2011. 5114

Boer, G. J., Flato, G., and Ramsden, D.: A transient climate change simulation with greenhouse gas and aerosol forcing: projected climate to the twenty-first century, Climate Dyn., 16, 427–450, doi:10.1007/s003820050338, 2000. 5134

Bollasina, M. A., Ming, Y., and Ramaswamy, V.: Anthropogenic aerosols and the weakening of

ACPD

12, 5107–5188, 2012

the South Asian summer monsoon, Science, 334, 502–505, doi:10.1126/science.1204994, 2011. 5110, 5111, 5129, 5130, 5135, 5140, 5147

Bond, T. C., Streets, D. G., Yarber, K. F., Nelson, S. M., Woo, J., and Klimont, Z.: A technology-based global inventory of black and organic carbon emissions from combustion, J. Geophys. Res., 109, D14203, doi:10.1029/2003JD003697, 2004. 5117

Boucher, O., Collier, M., Dufresne, J.-L., Forster, P., Haywood, J., Jeffrey, S., Jones, A., Lohmann, U., Rasch, P., Rotstayn, L., Stevens, B., Taylor, K., and von Salzen, K.: Climate response to aerosol forcings in CMIP5, CLIVAR Exchanges, 56, 25–27, http://www.clivar.org/publications/exchanges/Exchanges_56.pdf%, 2011. 5111, 5145

Brohan, P., Kennedy, J. J., Harris, I., Tett, S. F. B., and Jones, P. D.: Uncertainty estimates in regional and global observed temperature changes: A new data set from 1850, J. Geophys. Res., 111, D12106, doi:10.1029/2005JD006548, 2006. 5126

Cai, W., Sullivan, A., Cowan, T., Ribbe, J., and Shi, G.: Simulation of the Indian Ocean Dipole: A relevant criterion for selecting models for climate projections, Geophys. Res. Lett., 38, L3704, doi:10.1029/2010GL046242, 2011a. 5146

Cai, W., Cowan, T., Sullivan, A., Ribbe, J., and Shi, G.: Are anthropogenic aerosols responsible for the northwest Australia summer rainfall increase? A CMIP3 perspective and implications, J. Climate, 24, 2556–2564, doi:10.1175/2010JCLI3832.1, 2011b. 5113, 5129, 5145

Cakmur, R. V., Miller, R. L., Perlwitz, J., Geogdzhayev, I. V., Ginoux, P., Koch, D., Kohfeld, K. E., Tegen, I., and Zender, C. S.: Constraining the magnitude of the global dust cycle by minimizing the difference between a model and observations, J. Geophys. Res., 111, D6207, doi:10.1029/2005JD005791, 2006. 5118

Chen, J., Carlson, B. E., and Del Genio, A. D.: Evidence for Strengthening of the Tropical General Circulation in the 1990s, Science, 295, 838–841, doi:10.1126/science.1065835, 2002. 5110

Chou, C. and Neelin, J. D.: Mechanisms of Global Warming Impacts on Regional Tropical Precipitation, J. Climate, 17, 2688–2701, 2004. 5145

Chou, M.-D. and Lee, K.-T.: A Parameterization of the Effective Layer Emission for Infrared Radiation Calculations, J. Atmos. Sci., 62, 531–541, 2005. 5119

Cionni, I., Eyring, V., Lamarque, J. F., Randel, W. J., Stevenson, D. S., Wu, F., Bodeker, G. E., Shepherd, T. G., Shindell, D. T., and Waugh, D. W.: Ozone database in support of CMIP5 simulations: results and corresponding radiative forcing, Atmos. Chem. Phys., 11, 11267–11292, doi:10.5194/acp-11-11267-2011, 2011. 5121

ACPD
12, 5107–5188, 2012

Clarke, L., Edmonds, J., Jacoby, H., Pitcher, H., Reilly, J., and Richels, R.: Scenarios of Greenhouse Gas Emissions and Atmospheric Concentrations, Sub-report 2.1A of Synthesis and Assessment Product 2.1, Department of Energy, Washington, DC, USA, 154 pp., 2007. 5125

Cooke, W. F., Liousse, C., Cachier, H., and Feichter, J.: Construction of a 1° × 1° fossil fuel emission data set for carbonaceous aerosol and implementation and radiative impact in the ECHAM4 model, J. Geophys. Res., 104, 22137–22162, 1999. 5118

Cowan, T. and Cai, W.: The impact of Asian and non-Asian anthropogenic aerosols on 20th century Asian summer monsoon, Geophys. Res. Lett., 38, L11703, doi:10.1029/2011GL047268, 2011. 5132

Dee, D. P., Uppala, S. M., Simmons, A. J., Berrisford, P., Poli, P., Kobayashi, S., Andrae, U., Balmaseda, M. A., Balsamo, G., Bauer, P., Bechtold, P., Beljaars, A. C. M., van de Berg, L., Bidlot, J., Bormann, N., Delsol, C., Dragani, R., Fuentes, M., Geer, A. J., Haimberger, L., Healy, S. B., Hersbach, H., Holm, E. V., Isaksen, L., Kallberg, P., Koehler, M., Matricardi, M., McNally, A. P., Monge-Sanz, B. M., Morcrette, J. J., Park, B. K., Peubey, C., de Rosnay, P., Tavolato, C., Thepaut, J. N., and Vitart, F.: The ERA-Interim reanalysis: Configuration and performance of the data assimilation system, Q. J. Roy. Meteorol. Soc., 137, 553–597, doi:10.1002/qj.828, 2011. 5138

Dentener, F., Kinne, S., Bond, T., Boucher, O., Cofala, J., Generoso, S., Ginoux, P., Gong, S., Hoelzemann, J. J., Ito, A., Marelli, L., Penner, J. E., Putaud, J.-P., Textor, C., Schulz, M., van der Werf, G. R., and Wilson, J.: Emissions of primary aerosol and precursor gases in the years 2000 and 1750 prescribed data-sets for AeroCom, Atmos. Chem. Phys., 6, 4321–4344, doi:10.5194/acp-6-4321-2006, 2006. 5117

Deser, C., Phillips, A. S., and Alexander, M. A.: Twentieth century tropical sea surface temperature trends revisited, Geophys. Res. Lett., 37, L10701, doi:10.1029/2010GL043321, 2010. 5143

Deser, C., Phillips, A., Bourdette, V., and Teng, H.: Uncertainty in climate change projections: the role of internal variability, Climate Dyn., 38, 527–546, doi:10.1007/s00382-010-0977-x, 2012. 5129

DiNezio, P. N., Clement, A. C., Vecchi, G. A., Soden, B. J., Kirtman, B. P., and Lee, S.: Climate Response of the Equatorial Pacific to Global Warming, J. Climate, 22, 4873–4892, doi:10.1175/2009JCLI2982.1, 2009. 5134, 5136

Feichter, J., Kjellström, E., Rodhe, H., Dentener, F., Lelieveld, J., and Roelofs, G.-J.: Simulation of the tropospheric sulfur cycle in a global climate model, Atmos. Environ., 30, 1693–1707,

ACPD
12, 5107–5188, 2012

1996. 5118
Feichter, J., Roeckner, E., Lohmann, U., and Liepert, B.: Nonlinear aspects of the climate response to greenhouse gas and aerosol forcing, J. Climate, 17, 2384–2398, 2004. 5126
Feng, M., Biastoch, A., Böning, C., Caputi, N., and Meyers, G.: Seasonal and interannual variations of upper ocean heat balance off the west coast of Australia, J. Geophys. Res., 113, C12025, doi:10.1029/2008JC004908, 2008. 5128
Forster, P., Ramaswamy, V., Artaxo, P., Berntsen, T., Betts, R., Fahey, D., Haywood, J., Lean, J., Lowe, D., Myhre, G., Nganga, J., Prinn, R., Raga, G., Schulz, M., and Dorland, R. V.: Changes in Atmospheric Constituents and in Radiative Forcing, in: Climate Change 2007: The Physical Science Basis. Contribution of Working Group I to the Fourth Assessment Report of the Intergovernmental Panel on Climate Change, edited by: Solomon, S., Qin, D., Manning, M., Chen, Z., Marquis, M., Averyt, K. B., Tignor, M., and Miller, H. L., Cambridge University Press, Cambridge, United Kingdom and New York, NY, USA, 2007. 5109, 5123, 5146
Gill, A. E.: Some simple solutions for heat-induced tropical circulation, Q. J. Roy. Meteorol. Soc., 106, 447–462, doi:10.1256/smsqj.44904, 1980. 5139
Ginoux, P., Chin, M., Tegen, I., Prospero, J. M., Holben, B., Dubovik, O., and Lin, S.-J.: Sources and distributions of dust aerosols simulated with the GOCART model, J. Geophys. Res., 106, 20255–20273, doi:10.1029/2000JD000053, 2001. 5118, 5119
Ginoux, P., Prospero, J. M., Torres, O., and Chin, M.: Long-term simulation of global dust distribution with the GOCART model: correlation with North Atlantic Oscillation, Environ. Modell. Softw., 19, 113–128, 2004. 5118
Goldstein, A. H. and Galbally, I. E.: Known and unexplored organic constituents in the earth's atmosphere, Environ. Sci. Technol., 41, 1514–1521, 2007. 5118
Gordon, H. B.: A Flux Formulation of the Spectral Atmospheric Equations Suitable for Use in Long Term Climate Modeling, Mon. Weather Rev., 109, 56–64, 1981. 5115
Gordon, H. B., Rotstayn, L. D., McGregor, J. L., Dix, M. R., Kowalczyk, E. A., O'Farrell, S. P., Waterman, L. J., Hirst, A. C., Wilson, S. G., Collier, M. A., Watterson, I. G., and Elliott, T. I.: The CSIRO Mk3 Climate System Model, Technical Paper No. 60, CSIRO Atmospheric Research, Aspendale, Vic., Australia, 134 pp., available at: http://www.cmar.csiro.au/e-print/open/gordon_2002a.pdf, 2002. 5115, 5116
Gordon, H. B., O'Farrell, S. P., Collier, M. A., Dix, M. R., Rotstayn, L. D., Kowalczyk, E. A., Hirst, A. C., and Watterson, I. G.: The CSIRO Mk3.5 Climate Model, Technical Report No. 21,

ACPD
12, 5107–5188, 2012

The Centre for Australian Weather and Climate Research, Aspendale, Vic., Australia, 62 pp., available at: http://www.cawcr.gov.au/publications/technicalreports.php, 2010. 5115, 5116
Grant, K. E. and Grossman, A. S.: Description of a Solar Radiative Transfer Model for Use in LLNL Climate and Atmospheric Chemistry Studies, UCRL-ID- 129949, Lawrence Livermore National Laboratory, Livermore, CA, USA, available at: http://www.llnl.gov/tid/lof/documents/pdf/233048.pdf, 17 pp., 1998. 5119
Grant, K. E., Chuang, C. C., Grossman, A. S., and Penner, J. E.: Modeling the spectral optical properties of ammonium sulfate and biomass burning aerosols: parameterization of relative humidity effects and model results, Atmos. Environ., 33, 2603–2620, 1999. 5119
Gregory, D.: The representation of moist convection in atmospheric models, Climate Research Technical Note 54, Hadley Centre, 1995. 5115
Gregory, D. and Rowntree, P. R.: A mass flux convection scheme with representation of cloud ensemble characteristics and stability-dependent closure, Mon. Weather Rev., 118, 1483–1506, 1990. 5115, 5118
Guenther, A., Hewitt, C. N., Erickson, D., Fall, R., Geron, C., Graedel, T., Harley, P., Klinger, L., Lerdau, M., McKay, W. A., Pierce, T., Scholes, B., Steinbrecher, R., Tallamraju, R., Taylor, J., and Zimmerman, P.: A global model of natural volatile organic compound emissions, J. Geophys. Res., 100, 8873–8892, 1995. 5117
Han, W., Meehl, G. A., Rajagopalan, B., Fasullo, J. T., Hu, A., Lin, J., Large, W. G., Wang, J.-W., Quan, X.-W., Trenary, L. L., Wallcraft, A., Shinoda, T., and Yeager, S.: Patterns of Indian Ocean sea-level change in a warming climate, Nature Geosci., 3, 546–550, doi:10.1038/ngeo901, 2010. 5138
Hansen, J. and Nazarenko, L.: Soot climate forcing via snow and ice albedos, P. Natl. Acad. Sci., 101, 423–428, doi:10.1073/pnas.2237157100, 2004. 5121
Hansen, J., Sato, M., Nazarenko, L., Ruedy, R., Lacis, A., Koch, D., Tegen, I., Hall, T., Shindell, D., Santer, B., Stone, P., Novakov, T., Thomason, L., Wang, R., Wang, Y., Jacob, D., Hollandsworth, S., Bishop, L., Logan, J., Thompson, A., Stolarski, R., Lean, J., Willson, R., Levitus, S., Antonov, J., Rayner, N., Parker, D., and Christy, J.: Climate forcings in Goddard Institute for Space Studies SI2000 simulations, J. Geophys. Res., 107, 4737, doi:10.1029/2001JD001143, 2002. 5124
Hastenrath, S. and Polzin, D.: Dynamics of the surface wind field over the equatorial Indian Ocean, Q. J. Roy. Meteorol. Soc., 130, 503–517, doi:10.1256/qj.03.79, 2004. 5140
Held, I. M. and Soden, B. J.: Robust Responses of the Hydrological Cycle to Global Warming,

ACPD
12, 5107–5188, 2012

J. Climate, 19, 5686–5699, doi:10.1175/JCLI3990.1, 2006. 5110, 5135, 5145, 5147
Hendon, H. H.: Indonesian rainfall variability: Impacts of ENSO and local air-sea interaction, J. Climate, 16, 1775–1790, 2003. 5129
Hirst, A. C. and Godfrey, J. S.: The role of Indonesian throughflow in a global ocean GCM, J. Phys. Oceanogr., 23, 1057–1086, doi:10.1175/1520-0485(1993)023¡1057:TROITI¿2.0.CO;2, 1993. 5141
Holtslag, A. A. M. and Boville, B. A.: Local versus non-local boundary layer diffusion in a global climate model, J. Climate, 6, 1825–1842, 1993. 5115
Jathar, S. H., Farina, S. C., Robinson, A. L., and Adams, P. J.: The influence of semi-volatile and reactive primary emissions on the abundance and properties of global organic aerosol, Atmos. Chem. Phys., 11, 7727–7746, doi:10.5194/acp-11-7727-2011, 2011. 5166
Jones, A., Roberts, D. L., and Slingo, A.: A climate model study of indirect radiative forcing by anthropogenic sulphate aerosols, Nature, 370, 450–453, 1994. 5119
Jones, D. A., Wang, W., and Fawcett, R.: High-quality spatial climate data-sets for Australia, Aust. Meteorol. Oceanogr. J., 58, 233–248, 2009. 5112
Kajikawa, Y., Wang, B., and Yang, J.: A multi-time scale Australian monsoon index, Int. J. Climatol., 30, 1114–1120, doi:10.1002/joc.1955, 2010. 5141
Kalnay, E., Kanamitsu, M., Kistler, R., Collins, W., Deaven, D., Gandin, L., Iredell, M., Saha, S., White, G., Woollen, J., Zhu, Y., Chelliah, M., Ebisuzaki, W., Higgins, W., Janowiak, J., Mo, K. C., Ropelewski, C., Wang, J., Leetmaa, A., Reynolds, R., Jenne, R., and Joseph, D.: The NCEP/NCAR 40-year reanalysis project, B. Am. Meteorol. Soc., 77, 437–471, 1996. 5138
Kanakidou, M., Seinfeld, J. H., Pandis, S. N., Barnes, I., Dentener, F. J., Facchini, M. C., Van Dingenen, R., Ervens, B., Nenes, A., Nielsen, C. J., Swietlicki, E., Putaud, J. P., Balkanski, Y., Fuzzi, S., Horth, J., Moortgat, G. K., Winterhalter, R., Myhre, C. E. L., Tsigaridis, K., Vignati, E., Stephanou, E. G., and Wilson, J.: Organic aerosol and global climate modelling: a review, Atmos. Chem. Phys., 5, 1053–1123, doi:10.5194/acp-5-1053-2005, 2005. 5117, 5118
Kanamitsu, M., Ebisuzaki, W., Woollen, J., Yang, S. K., Hnilo, J. J., Fiorino, M., and Potter, G. L.: NCEP-DOE AMIP-II reanalysis (R-2), B. Am. Meteorol. Soc., 83, 1631–1643, doi:10.1175/BAMS-83-11-1631, 2002. 5127, 5138
Kang, S. M., Polvani, L. M., Fyfe, J. C., and Sigmond, M.: Impact of polar ozone depletion on subtropical precipitation, Science, 332, 951–954, doi:10.1126/science.1202131, 2011. 5131, 5132

ACPD
12, 5107–5188, 2012

Kawase, H., Abe, M., Yamada, Y., Takemura, T., Yokohata, T., and Nozawa, T.: Physical mechanism of long-term drying trend over tropical North Africa, Geophys. Res. Lett., 37, L09706, doi:10.1029/2010GL043038, 2010. 5111

Kettle, A. J. and Andreae, M. O.: Flux of dimethylsulfide from the oceans: A comparison of updated data sets and flux models, J. Geophys. Res., 105, 26793–26808, 2000. 5117

Kettle, A. J., Andreae, M. O., Amouroux, D., Andreae, T. W., Bates, T. S., Berresheim, H., Bingemer, H., Boniforti, R., Curran, M. A. J., DiTullio, G. R., Helas, G., Jones, G. B., Keller, M. D., Kiene, R. P., Leck, C., Levasseur, M., Malin, G., Maspero, M., Matrai, P., McTaggart, A. R., Mihalopoulos, N., Nguyen, B. C., Novo, A., Putaud, J. P., Rapsomanikis, S., Roberts, G., Schebeske, G., Sharma, S., Simo, R., Staubes, R., Turner, S., and Uher, G.: A global database of sea surface dimethylsulfide (DMS) measurements and a procedure to predict sea surface DMS as a function of latitude, longitude and month, Global Biogeochem. Cy., 13, 399–444, 1999. 5117

Kinne, S., Schulz, M., Textor, C., Guibert, S., Balkanski, Y., Bauer, S. E., Berntsen, T., Berglen, T. F., Boucher, O., Chin, M., Collins, W., Dentener, F., Diehl, T., Easter, R., Feichter, J., Fillmore, D., Ghan, S., Ginoux, P., Gong, S., Grini, A., Hendricks, J., Herzog, M., Horowitz, L., Isaksen, I., Iversen, T., Kirkevåg, A., Kloster, S., Koch, D., Kristjansson, J. E., Krol, M., Lauer, A., Lamarque, J. F., Lesins, G., Liu, X., Lohmann, U., Montanaro, V., Myhre, G., Penner, J., Pitari, G., Reddy, S., Seland, O., Stier, P., Takemura, T., and Tie, X.: An AeroCom initial assessment – optical properties in aerosol component modules of global models, Atmos. Chem. Phys., 6, 1815–1834, doi:10.5194/acp-6-1815-2006, 2006. 5123, 5166

Klein, S. A., Soden, B. J., and Lau, N. C.: Remote sea surface temperature variations during ENSO: Evidence for a tropical atmospheric bridge, J. Climate, 12, 917–932, 1999. 5128

Kloster, S., Dentener, F., Feichter, J., Raes, F., Lohmann, U., Roeckner, E., and Fischer-Bruns, I.: A GCM study of future climate response to aerosol pollution reductions, Climate Dyn., 34, 1177–1194, doi:10.1007/s00382-009-0573-0, 2010. 5110

Knutson, T. R. and Manabe, S.: Time-Mean Response over the Tropical Pacific to Increased $C0_2$ in a Coupled Ocean-Atmosphere Model, J. Climate, 8, 2181–2199, 1995. 5110

Kraus, E. B. and Turner, J.: A one dimensional model of the seasonal thermocline II. The general theory and its consequences, Tellus, 19, 98–106, 1967. 5116

Kristjánsson, J. E., Iversen, T., Kirkevåg, A., Seland, Ø., and Debernard, J.: Response of the climate system to aerosol direct and indirect forcing: Role of cloud feedbacks, J. Geophys. Res., 110, D24206, doi:10.1029/2005JD006299, 2005. 5111

ACPD
12, 5107–5188, 2012

Lamarque, J.-F., Bond, T. C., Eyring, V., Granier, C., Heil, A., Klimont, Z., Lee, D., Liousse, C., Mieville, A., Owen, B., Schultz, M. G., Shindell, D., Smith, S. J., Stehfest, E., Van Aardenne, J., Cooper, O. R., Kainuma, M., Mahowald, N., McConnell, J. R., Naik, V., Riahi, K., and van Vuuren, D. P.: Historical (1850–2000) gridded anthropogenic and biomass burning emissions of reactive gases and aerosols: methodology and application, Atmos. Chem. Phys., 10, 7017–7039, doi:10.5194/acp-10-7017-2010, 2010. 5116, 5121, 5122, 5124, 5126

Lana, A., Bell, T. G., Simó, R., Vallina, S. M., Ballabrera-Poy, J., Kettle, A. J., Dachs, J., Bopp, L., Saltzman, E. S., Stefels, J., Johnson, J. E., and Liss, P. S.: An updated climatology of surface dimethlysulfide concentrations and emission fluxes in the global ocean, Glob. Biogeochem. Cy., 25, GB1004, doi:10.1029/2010GB003850, 2011. 5117

Latif, M., Sperber, K., Arblaster, J., Braconnot, P., Chen, D., Colman, A., Cubasch, U., Cooper, C., Delecluse, P., Dewitt, D., Fairhead, L., Flato, G., Hogan, T., Ji, M., Kimoto, M., Kitoh, A., Knutson, T., Le Treut, H., Li, T., Manabe, S., Marti, O., Mechoso, C., Meehl, G., Power, S., Roeckner, E., Sirven, J., Terray, L., Vintzileos, A., Voß, R., Wang, B., Washington, W., Yoshikawa, I., Yu, J., and Zebiak, S.: ENSIP: the El Niño simulation intercomparison project, Climate Dyn., 18, 255–276, doi:10.1007/s003820100174, 2001. 5113

Lau, N. C. and Nath, M. J.: Impact of ENSO on the variability of the Asian-Australian monsoons as simulated in GCM experiments, J. Climate, 13, 4287–4309, doi:10.1175/1520-0442(2000)013¡4287:IOEOTV¿2.0.CO;2, 2000. 5128, 5148

Lean, J.: Evolution of the Sun's spectral irradiance since the Maunder Minimum, Geophys. Res. Lett., 27, 2425–2428, doi:10.1029/2000GL000043, 2000. 5121

Lee, S., Kim, H. K., Yan, B., Cobb, C. E., Hennigan, C., Nichols, S., Chamber, M., Edgerton, E. S., Jansen, J. J., Hu, Y., Zheng, M., Weber, R. J., and Russell, A. G.: Diagnosis of Aged Prescribed Burning Plumes Impacting an Urban Area, Environ. Sci. Technol., 42, 1438–1444, doi:10.1021/es7023059, 2008. 5117

Liepert, B. G., Feichter, J., Lohmann, U., and Roeckner, E.: Can aerosols spin down the water cycle in a warmer and moister world?, Geophys. Res. Lett., 31, L06207, doi:10.1029/2003GL019060, 2004. 5110

Lin, J.-L.: The double-ITCZ problem in IPCC AR4 coupled GCMs: Ocean-atmosphere feedback analysis, J. Climate, 20, 4497–4525, doi:10.1175/JCLI4272.1, 2007. 5127

Lin, Z. and Li, Y.: Remote influence of the tropical Atlantic on the variability and trend in North West Australia summer rainfall, J. Climate, doi:10.1175/JCLI-D-11-00020.1, in press, 2012. 5114, 5145

ACPD
12, 5107–5188, 2012

Lindzen, R. S. and Nigam, S.: On the Role of Sea Surface Temperature Gradients in Forcing Low-Level Winds and Convergence in the Tropics., J. Atmos. Sci., 44, 2418–2436, doi:10.1175/1520-0469(1987)044¡2418:OTROSS¿2.0.CO;2, 1987. 5133, 5143

Liss, P. S. and Merlivat, L.: Air-sea gas exchange rates: Introduction and synthesis, in: The role of air-sea gas exchange in geochemical cycling, edited by: Menard, P. B., 113–127, D. Reidel, Norwell, Mass., 1986. 5117

Liu, X., Penner, J. E., and Herzog, M.: Global modeling of aerosol dynamics: Model description, evaluation, and interactions between sulfate and nonsulfate aerosols, J. Geophys. Res., 110, D18206, doi:10.1029/2004JD005674, 2005a. 5166

Liu, Z., Vavrus, S., He, F., Wen, N., and Zhong, Y.: Rethinking Tropical Ocean Response to Global Warming: The Enhanced Equatorial Warming, J. Climate, 18, 4684–4700, doi:10.1175/JCLI3579.1, 2005b. 5134

Lohmann, U., Feichter, J., Chuang, C. C., and Penner, J. E.: Prediction of the number of cloud droplets in the ECHAM GCM, J. Geophys. Res., 104, 9169–9198, 1999. 5119

Lohmann, U., Rotstayn, L., Storelvmo, T., Jones, A., Menon, S., Quaas, J., Ekman, A. M. L., Koch, D., and Ruedy, R.: Total aerosol effect: radiative forcing or radiative flux perturbation?, Atmos. Chem. Phys., 10, 3235–3246, doi:10.5194/acp-10-3235-2010, 2010. 5124

Louis, J.-F.: A Parametric Model of Vertical Eddy Fluxes in the Atmosphere, Bound. Lay. Meteorol., 17, 187–202, 1979. 5115

Lu, J., Chen, G., and Frierson, D. M. W.: Response of the Zonal Mean Atmospheric Circulation to El Nino versus Global Warming, J. Climate, 21, 5835–5851, doi:10.1175/2008JCLI2200.1, 2008. 5128, 5137

Luffman, J. J., Taschetto, A. S., and England, M. H.: Global and Regional Climate Response to Late Twentieth-Century Warming over the Indian Ocean, J. Climate, 23, 1660–1674, doi:10.1175/2009JCLI3086.1, 2010. 5113

Matsuno, T.: Quasi-geostrophic motions in the equatorial area, J. Meteorol. Soc. Japan, 44, 25–43, 1966. 5139

McGregor, J. L.: Economical Determination of Departure Points for Semi-Lagrangian Models, Mon. Weather Rev., 121, 221–230, 1993. 5115

Meehl, G. A., Stocker, T. F., Collins, W. D., Friedlingstein, P., Gaye, A. T., Gregory, J. M., Kitoh, A., Knutti, R., Murphy, J. M., Noda, A., Raper, S. C. B., Watterson, I., Weaver, A. J., and Zhao, Z.-C.: Global Change Projections, in: Climate Change 2007: The Physical Science Basis. Contribution of Working Group I to the Fourth Assessment Report of the Intergovernmental

ACPD
12, 5107–5188, 2012

Panel on Climate Change, edited by: Solomon, S., Qin, D., Manning, M., Chen, Z., Marquis, M., Averyt, K. B., Tignor, M., and Miller, H. L., Cambridge University Press, Cambridge, United Kingdom and New York, NY, USA, 2007. 5129, 5134
Meehl, G. A., Arblaster, J. M., and Collins, W. D.: Effects of Black Carbon Aerosols on the Indian Monsoon, J. Climate, 21, 2869–2882, doi:10.1175/2007JCLI1777.1, 2008. 5111
Meyers, G.: Variation of Indonesian Throughflow and the El Niño-Southern Oscillation, J. Geophys. Res., 101, 12255–12264, doi:10.1029/95JC03729, 1996. 5141
Ming, Y. and Ramaswamy, V.: Nonlinear climate and hydrological responses to aerosol effects, J. Climate, 22, 1329–1339, doi:10.1175/2008JCLI2362.1, 2009. 5126
Ming, Y. and Ramaswamy, V.: A model investigation of aerosol-induced changes in tropical circulation, J. Climate, 24, 5125–5133, doi:10.1175/2011JCLI4108.1, 2011. 5110, 5147
Mitas, C. M. and Clement, A.: Has the Hadley cell been strengthening in recent decades, Geophys. Res. Lett, 32, L3809, doi:10.1029/2004GL021765, 2005. 5144
Moss, R. H., Edmonds, J. A., Hibbard, K. A., Manning, M. R., Rose, S. K., van Vuuren, D. P., Carter, T. R., Emori, S., Kainuma, M., Kram, T., Meehl, G. A., Mitchell, J. F. B., Nakicenovic, N., Riahi, K., Smith, S. J., Stouffer, R. J., Thomson, A. M., Weyant, J. P., and Wilbanks, T. J.: The next generation of scenarios for climate change research and assessment, Nature, 463, 747–756, doi:10.1038/nature08823, 2010. 5121
Moura, A. D. and Shukla, J.: On the Dynamics of Droughts in Northeast Brazil: Observations, Theory and Numerical Experiments with a General Circulation Model., J. Atmos. Sci., 38, 2653–2675, doi:10.1175/1520-0469(1981)038¡2653:OTDODI¿2.0.CO;2, 1981. 5139, 5143
Myhre, G.: Consistency Between Satellite-Derived and Modeled Estimates of the Direct Aerosol Effect, Science, 325, 187–190, doi:10.1126/science.1174461, 2009. 5124
Nightingale, P. D., Malin, G., Law, C. S., Watson, A. J., Liss, P. S., Liddicoat, M. I., Boutin, J., and Upstill-Goddard, R. C.: In situ evaluation of air-sea gas exchange parameterizations using novel conservative and volatile tracers, Global Biogeochem. Cy., 14, 373–387, 2000. 5117
O'Dowd, C. D., Smith, M. H., Consterdine, I. E., and Lowe, J. A.: Marine aerosol, sea-salt, and the marine sulphur cycle: a short review, Atmos. Environ., 31, 73–80, 1997. 5116, 5120
O'Farrell, S. P.: Investigation of the dynamic sea ice component of a coupled atmosphere-sea ice general circulation model, J. Geophys. Res., 103, 15751–15782, 1998. 5116
Pacanowski, R. C.: MOM 2 Version 2, Documentation, User's Guide and Reference Manual, GFDL Ocean Technical Report 3.2, Geophysical Fluid Dynamics Laboratory/NOAA,

ACPD
12, 5107–5188, 2012

Princeton, NJ, USA, available at: http://www.gfdl.noaa.gov/cms-filesystem-action?file=model_development/ocean/manual2.2.pdf, 1996. 5116
Parker, D., Folland, C., Scaife, A., Knight, J., Colman, A., Baines, P., and Dong, B.: Decadal to multidecadal variability and the climate change background, J. Geophys. Res., 112, D18115, doi:10.1029/2007JD008411, 2007. 5144
Penner, J. E., Chuang, C. C., and Grant, K.: Climate forcing by carbonaceous and sulfate aerosols, Climate Dyn., 14, 839–851, 1998. 5116
Power, S., Casey, T., Folland, C., Colman, A., and Mehta, V.: Inter-decadal modulation of the impact of ENSO on Australia, Climate Dyn., 15, 319–324, doi:10.1007/s003820050284, 1999. 5144
Prospero, J. M., Ginoux, P., Torres, O., Nicholson, S. E., and Gill, T. E.: Environmental characterization of global sources of atmospheric soil dust identified with the NIMBUS 7 Total Ozone Mapping Spectrometer (TOMS) absorbing aerosol product, Rev. Geophys., 40, 1002, doi:10.1029/2000RG000095, 2002. 5118
Lohmann, U., Rotstayn, L., Storelvmo, T., Jones, A., Menon, S., Quaas, J., Ekman, A. M. L., Koch, D., and Ruedy, R.: Total aerosol effect: radiative forcing or radiative flux perturbation?, Atmos. Chem. Phys., 10, 3235–3246, doi:10.5194/acp-10-3235-2010, 2010. 5118
Ramanathan, V., Chung, C., Kim, D., Bettge, T., Buja, L., Kiehl, J. T., Washington, W. M., Fu, Q., Sikka, D. R., and Wild, M.: Atmospheric Brown Clouds: Impacts on South Asian Climate and Hydrological Cycle, P. Natl. Acad. Sci., 102, 5326–5333, 2005. 5111
Rayner, N. A., Parker, D. E., Horton, E. B., Folland, C. K., Alexander, L. V., Rowell, D. P., Kent, E. C., and Kaplan, A.: Globally complete analyses of sea surface temperature, sea ice and night marine air temperature, J. Geophys. Res., 108, 4407, doi:10.1029/2002JD002670, 2003. 5128
Remer, L. A., Kleidman, R. G., Levy, R. C., Kaufman, Y. J., Tanre, D., Mattoo, S., Martins, J. V., Ichoku, C., Koren, I., Yu, H., and Holben, B. N.: Global aerosol climatology from the MODIS satellite sensors, J. Geophys. Res., 113, D14S07, doi:10.1029/2007JD009661, 2008. 5123
Roberts, D. L. and Jones, A.: Climate sensitivity to black carbon aerosol from fossil fuel combustion, J. Geophys. Res., 109, D16202, doi:10.1029/2004JD004676, 2004. 5111
Rodwell, M. J. and Hoskins, B. J.: Subtropical anticyclones and summer monsoons, J. Climate, 14, 3192–3211, doi:10.1175/1520-0442(2001)014¡3192:SAASM¿2.0.CO;2, 2001. 5137
Roeckner, E., Stier, P., Feichter, J., Kloster, S., Esch, M., and Fischer-Bruns, I.: Impact of carbonaceous aerosol emissions on regional climate change, Clim. Dyn., 27, 553–571,

ACPD
12, 5107–5188, 2012

doi:10.1007/s00382-006-0147-3, 2006. 5111
Rotstayn, L. D.: A physically based scheme for the treatment of stratiform clouds and precipitation in large-scale models. I: Description and evaluation of the microphysical processes, Q. J. Roy. Meteorol. Soc., 123, 1227–1282, 1997. 5115
Rotstayn, L. D.: A physically based scheme for the treatment of stratiform clouds and precipitation in large-scale models. II: Comparison of modelled and observed climatological fields, Q. J. Roy. Meteorol. Soc., 124, 389–415, 1998. 5115
Rotstayn, L. D.: On the "tuning" of autoconversion parameterizations in climate models, J. Geophys. Res., 105, 15495–15507, 2000. 5120
Rotstayn, L. D. and Liu, Y.: A smaller global estimate of the second indirect aerosol effect, Geophys. Res. Lett., 32, L05708, doi:10.1029/2004GL021922, 2005. 5120
Rotstayn, L. D. and Liu, Y.: Cloud droplet spectral dispersion and the indirect aerosol effect: Comparison of two treatments in a GCM, Geophys. Res. Lett., 36, L10801, doi:10.1029/2009GL038216, 2009. 5120
Rotstayn, L. D. and Lohmann, U.: Tropical Rainfall Trends and the Indirect Aerosol Effect, J. Climate, 15, 2103–2116, 2002a. 5110
Rotstayn, L. D. and Lohmann, U.: Simulation of the tropospheric sulfur cycle in a global model with a physically based cloud scheme, J. Geophys. Res., 107, 4592, doi:10.1029/2002JD002128, 2002b. 5117, 5118, 5119
Rotstayn, L. D. and Penner, J. E.: Indirect aerosol forcing, quasi-forcing and climate response, J. Climate, 14, 2960–2975, 2001. 5124
Rotstayn, L. D., Ryan, B. F., and Katzfey, J. J.: A scheme for calculation of the liquid fraction in mixed-phase stratiform clouds in large-scale models, Mon. Weather Rev., 128, 1070–1088, 2000a. 5115
Rotstayn, L. D., Ryan, B. F., and Penner, J. E.: Precipitation changes in a GCM resulting from the indirect effects of anthropogenic aerosols, Geophys. Res. Lett., 27, 3045–3048, 2000b. 5111
Rotstayn, L. D., Cai, W., Dix, M. R., Farquhar, G. D., Feng, Y., Ginoux, P., Herzog, M., Ito, A., Penner, J. E., Roderick, M. L., and Wang, M.: Have Australian Rainfall and Cloudiness Increased Due to the Remote Effects of Asian Anthropogenic Aerosols?, J. Geophys. Res., 112, D09202, doi:10.1029/2006JD007712, 2007. 5111, 5112, 5117, 5119, 5120, 5130, 5132, 5148
Rotstayn, L. D., Collier, M. A., Feng, Y., Gordon, H. B., O'Farrell, S. P., Smith, I. N., and Syktus,

ACPD
12, 5107–5188, 2012

J.: Improved simulation of Australian climate and ENSO-related rainfall variability in a GCM with an interactive aerosol treatment, Int. J. Climatol., 30, 1067–1088, doi:10.1002/joc.1952, 2010. 5115, 5117, 5127

Rotstayn, L. D., Collier, M. A., Mitchell, R. M., Qin, Y., Campbell, S. K., and Dravitzki, S. M.: Simulated enhancement of ENSO-related rainfall variability due to Australian dust, Atmos. Chem. Phys., 11, 6575–6592, doi:10.5194/acp-11-6575-2011, 2011. 5117, 5118, 5119, 5123

Saji, N. H., Goswami, B. N., Vinayachandran, P. N., and Yamagata, T.: A dipole mode in the tropical Indian Ocean, Nature, 401, 360–363, 1999. 5136

Sato, M., Hansen, J. E., McCormick, M. P., and Pollack, J. B.: Stratospheric aerosol optical depth, 1850–1990, J. Geophys. Res., 98, 22987–22994, 1993. 5116, 5121

Schneider, N.: The Indonesian Throughflow and the global climate system., J. Climate, 11, 676–689, doi:10.1175/1520-0442(1998)011¡0676:TITATG¿2.0.CO;2, 1998. 5141

Schott, F. A., Xie, S.-P., and McCreary, J. P.: Indian Ocean circulation and climate variability, Rev. Geophysics, 47, RG1002, doi:10.1029/2007RG000245, 2009. 5136

Schulz, M., Textor, C., Kinne, S., Balkanski, Y., Bauer, S., Berntsen, T., Berglen, T., Boucher, O., Dentener, F., Guibert, S., Isaksen, I. S. A., Iversen, T., Koch, D., Kirkevåg, A., Liu, X., Montanaro, V., Myhre, G., Penner, J. E., Pitari, G., Reddy, S., Seland, Ø., Stier, P., and Takemura, T.: Radiative forcing by aerosols as derived from the AeroCom present-day and pre-industrial simulations, Atmos. Chem. Phys., 6, 5225–5246, doi:10.5194/acp-6-5225-2006, 2006. 5122, 5123

Shi, G., Cai, W., Cowan, T., Ribbe, J., Rotstayn, L., and Dix, M.: Variability and trend of north west Australia rainfall: observations and coupled climate modeling, J. Climate, 21, 2938–2959, 2008. 5112, 5145

Smith, T. M., Reynolds, R. W., Peterson, T. C., and Lawrimore, J.: Improvements to NOAA's historical merged land-ocean surface temperature analysis (1880–2006), J. Climate, 21, 2283–2296, doi:10.1175/2007JCLI2100.1, 2008. 5143

Song, H. and Zhang, M.: Changes of the Boreal Winter Hadley Circulation in the NCEP NCAR and ECMWF Reanalyses: A Comparative Study, J. Climate, 20, 5191–5200, doi:10.1175/JCLI4260.1, 2007. 5144

Taschetto, A. S., Sen Gupta, A., Hendon, H. H., Ummenhofer, C. C., and England, M. H.: The Contribution of Indian Ocean Sea Surface Temperature Anomalies on Australian Summer Rainfall during El Nino Events, J. Climate, 24, 3734–3747, doi:10.1175/2011JCLI3885.1,

ACPD
12, 5107–5188, 2012

2011. 5128, 5148
Taylor, K. E., Stouffer, R. J., and Meehl, G. A.: A Summary of the CMIP5 Experiment Design, available at: http://cmip-pcmdi.llnl.gov/cmip5/docs/Taylor_CMIP5_design.pdf, 2009. 5111, 5121, 5123, 5125
Taylor, K. E., Stouffer, R. J., and Meehl, G. A.: An Overview of CMIP5 and the Experiment Design, B. Am. Meteorol. Soc., doi:10.1175/BAMS-D-11-00094.1, in press, 2012. 5111, 5121
Textor, C., Schulz, M., Guibert, S., Kinne, S., Balkanski, Y., Bauer, S., Berntsen, T., Berglen, T., Boucher, O., Chin, M., Dentener, F., Diehl, T., Easter, R., Feichter, H., Fillmore, D., Ghan, S., Ginoux, P., Gong, S., Grini, A., Hendricks, J., Horowitz, L., Huang, P., Isaksen, I., Iversen, I., Kloster, S., Koch, D., Kirkevåg, A., Kristjansson, J. E., Krol, M., Lauer, A., Lamarque, J. F., Liu, X., Montanaro, V., Myhre, G., Penner, J., Pitari, G., Reddy, S., Seland, Ø., Stier, P., Takemura, T., and Tie, X.: Analysis and quantification of the diversities of aerosol life cycles within AeroCom, Atmos. Chem. Phys., 6, 1777–1813, doi:10.5194/acp-6-1777-2006, 2006. 5122
Tokinaga, H., Xie, S.-P., Timmermann, A., McGregor, S., Ogata, T., Kubota, H., and Okumura, Y. M.: Regional patterns of tropical Indo-Pacific climate change: Evidence of the Walker Circulation weakening, J. Climate, doi:10.1175/JCLI-D-11-00263.1, in press, 2012. 5138
Trenary, L. L. and Han, W.: Causes of decadal subsurface cooling in the tropical Indian Ocean during 1961–2000, Geophys. Res. Lett., 35, L17602, doi:10.1029/2008GL034687, 2008. 5138
Van Leer, B.: Towards the Ultimate Conservative Difference Scheme. V. A New Approach to Numerical Convection, J. Comp. Phys., 23, 276–299, 1977. 5115
Vecchi, G. A. and Soden, B. J.: Global Warming and the Weakening of the Tropical Circulation, J. Climate, 20, 4316–4340, doi:10.1175/JCLI4258.1, 2007. 5110, 5127, 5135, 5136
Vecchi, G. A., Soden, B. J., Wittenberg, A. T., Held, I. M., Leetmaa, A., and Harrison, M. J.: Weakening of tropical Pacific atmospheric circulation due to anthropogenic forcing, Nature, 441, 73–76, doi:10.1038/nature04744, 2006. 5110
Visbeck, M., Marshall, J., Haine, T., and Spall, M.: Specification of eddy transfer coefficients in coarse-resolution ocean circulation models, J. Phys. Oceanogr., 27, 381–402, doi:10.1175/1520-0485(1997)027¡0381:SOETCI¿2.0.CO;2, 1997. 5116
Wang, B., Wu, R., and Fu, X.: Pacific-East Asian Teleconnection: How Does ENSO Affect East Asian Climate?, J. Climate, 13, 1517–1536, doi:10.1175/1520-

ACPD
12, 5107–5188, 2012

0442(2000)013¡1517:PEATHD¿2.0.CO;2, 2000. 5139
Wang, B., Wu, R. G., and Li, T.: Atmosphere-warm ocean interaction and its impacts on Asian-Australian monsoon variation, J. Climate, 16, 1195–1211, doi:10.1175/1520-0442(2003)16¡1195:AOIAII¿2.0.CO;2, 2003. 5128, 5135, 5137, 5143, 5148
Wang, B., Lee, J.-Y., Kang, I. S., Shukla, J., Kug, J. S., Kumar, A., Schemm, J., Luo, J. J., Yamagata, T., and Park, C. K.: How accurately do coupled climate models predict the leading modes of Asian-Australian monsoon interannual variability?, Climate Dyn., 30, 605–619, doi:10.1007/s00382-007-0310-5, 2008. 5128, 5148
Wang, Y.-M., Lean, J. L., and Sheeley, Jr., N. R.: Modeling the Sun's Magnetic Field and Irradiance since 1713, Astrophys. J., 625, 522–538, doi:10.1086/429689, 2005. 5121
Wardle, R. and Smith, I. N.: Modeled response of the Australian monsoon to changes in land surface temperatures, Geophys. Res. Lett., 31, L16205, doi:10.1029/2004GL020157, 2004. 5112
Watterson, I. G.: Relationships between southeastern Australian rainfall and sea surface temperatures examined using a climate model, J. Geophys. Res., 115, D10108, doi:10.1029/2009JD012120, 2010. 5133
Watterson, I. G.: Understanding and partitioning future climates for Australian regions from CMIP3 using ocean warming indices, Climatic Change, doi:10.1007/s10584-011-0166-x, in press, 2012. 5145
Wentz, F. J., Ricciardulli, L., Hilburn, K., and Mears, C.: How Much More Rain Will Global Warming Bring?, Science, 317, 233–235, doi:10.1126/science.1140746, 2007. 5110
Williams, K. D., Jones, A., Roberts, D. L., Senior, C. A., and Woodage, M. J.: The response of the climate system to the indirect effects of anthropogenic sulfate aerosol, Climate Dyn., 17, 845–856, 2001. 5111
Woodruff, S. D., Worley, S. J., Lubker, S. J., Ji, Z., Freeman, J. E., Berry, D. I., Brohan, P., Kent, E. C., Reynolds, R. W., Smith, S. R., and Wilkinson, C.: ICOADS Release 2.5: extensions and enhancements to the surface marine meteorological archive, Int. J. Climatol., 31, 951–967, doi:10.1002/joc.2103, 2011. 5144
Wu, B., Li, T., and Zhou, T.: Relative Contributions of the Indian Ocean and Local SST Anomalies to the Maintenance of the Western North Pacific Anomalous Anticyclone during the El Niño Decaying Summer, J. Climate, 23, 2974–2986, doi:10.1175/2010JCLI3300.1, 2010. 5143
Wu, R. G., Kinter, J. L., and Kirtman, B. P.: Discrepancy of interdecadal changes in the Asian

ACPD
12, 5107–5188, 2012

region among the NCEP-NCAR reanalysis, objective analyses, and observations, J. Climate, 18, 3048–3067, doi:10.1175/JCLI3465.1, 2005. 5138

Xie, S.-P., Deser, C., Vecchi, G. A., Ma, J., Teng, H., and Wittenberg, A. T.: Global Warming Pattern Formation: Sea Surface Temperature and Rainfall, J. Climate, 23, 966–986, doi:10.1175/2009JCLI3329.1, 2010. 5130, 5133, 5134, 5136

Zar, J. H.: Biostatistical Analysis, 3rd Edition, Prentice Hall International, London, 929 pp., 1996. 5129

Zender, C. S., Miller, R. L., and Tegen, I.: Quantifying mineral dust mass budgets: terminology, constraints, and current estimates, Eos, 85, 509–512, doi:10.1029/2004EO480002, 2004. 5166

Zhang, C. and Zhang, H.: Potential impacts of East Asian winter monsoon on climate variability and predictability in the Australian summer monsoon region, Theor. Appl. Climatol., 101, 161–177, doi:10.1007/s00704-009-0246-2, 2010. 5114

Zhang, H.: Diagnosing Australia-Asian monsoon onset/retreat using large-scale wind and moisture indices, Climate Dyn., 35, 601–618, doi:10.1007/s00382-009-0620-x, 2010. 5113

Zhang, M. and Song, H.: Evidence of deceleration of atmospheric vertical overturning circulation over the tropical Pacific, Geophys. Res. Lett., 331, L12701, doi:10.1029/2006GL025942, 2006. 5135

ACPD

12, 5107–5188, 2012

Table 1. Comparison of global-mean dry aerosol column burden (in mg m^{-2}) from the years 1850 and 2000 of the HIST ensemble with a modern-day reference range from other models.

	CSIRO-Mk3.6 1850	CSIRO-Mk3.6 2000	Reference range 2000
Sulfate	2.7	6.0	1.2–6.3[a]
OA	5.2	6.8	0.9–6.7[b]
BC	0.24	0.57	0.09–1.0[c]
Dust	69.9	71.0	16–71[d]
Sea salt	12.8	12.8	4.8–25.8[e]

[a] Liu et al. (2005a); Kinne et al. (2006), [b] Kinne et al. (2006); Jathar et al. (2011), [c] Kinne et al. (2006), [d] Zender et al. (2004); Kinne et al. (2006), [e] Kinne et al. (2006).

ACPD
12, 5107–5188, 2012

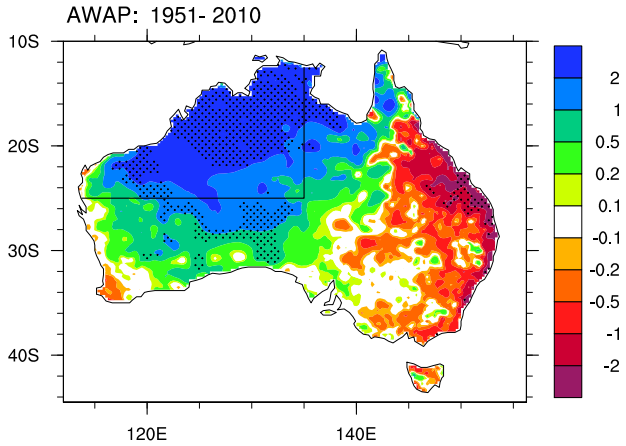

Fig. 1. Observed DJFM rainfall trends from AWAP (mm day^{-1} century^{-1}) for 1951–2010. Stippled trends are significant at 5 % based on a t-test, after adjusting for the serial correlation. The area enclosed by the black lines (land only) denotes the region referred to as north-western Australia in some of the following analysis.

ACPD
12, 5107–5188, 2012

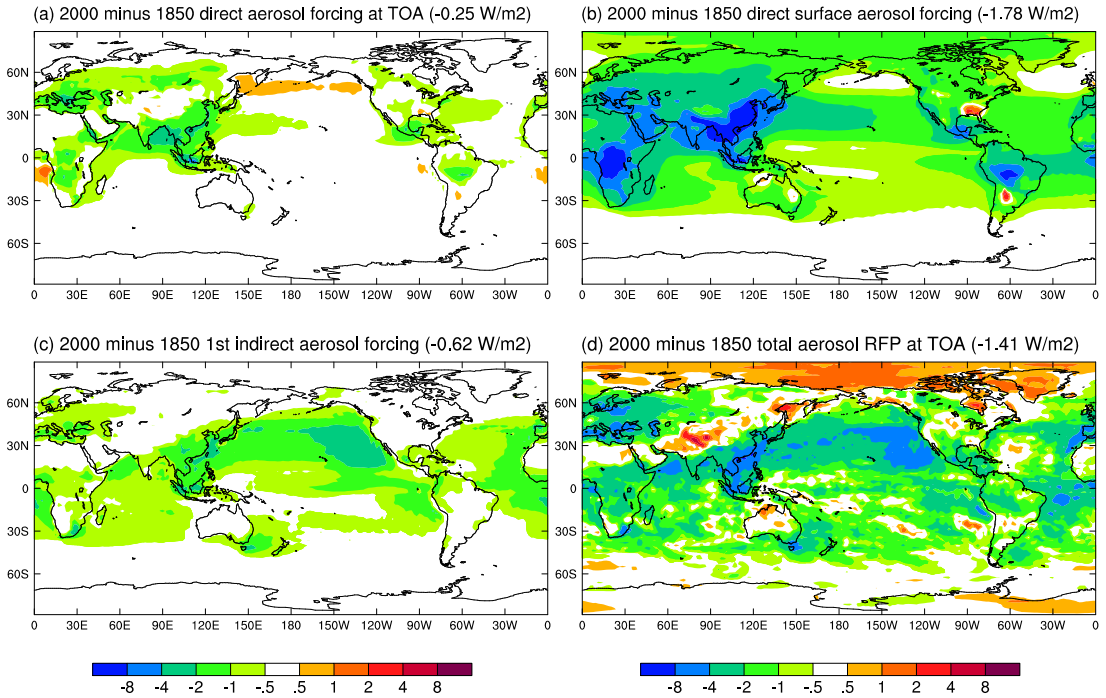

Fig. 2. Anthropogenic aerosol forcing (calculated as the difference between 2000 and 1850) in $W\,m^{-2}$: **(a)** direct effect at TOA, **(b)** direct effect at the surface, **(c)** first indirect effect at the TOA, **(d)** total aerosol radiative flux perturbation at TOA. The global-mean value for each plot is shown in its header.

ACPD
12, 5107–5188, 2012

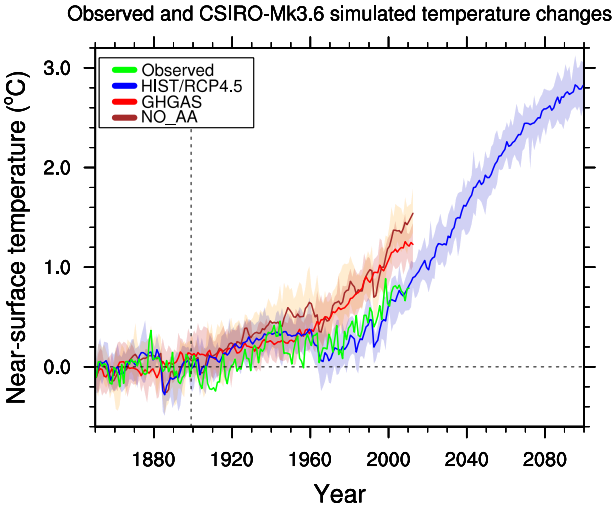

Fig. 3. Anomalies of annual, global-mean near-surface temperature from observations and the model (comprising SST over oceans, and near-surface air temperature over land). Solid lines show the ensemble mean, and shading shows the range of individual runs within each ensemble. Observations and the model both use their own 1850–1899 mean in the calculation of anomalies.

ACPD
12, 5107–5188, 2012

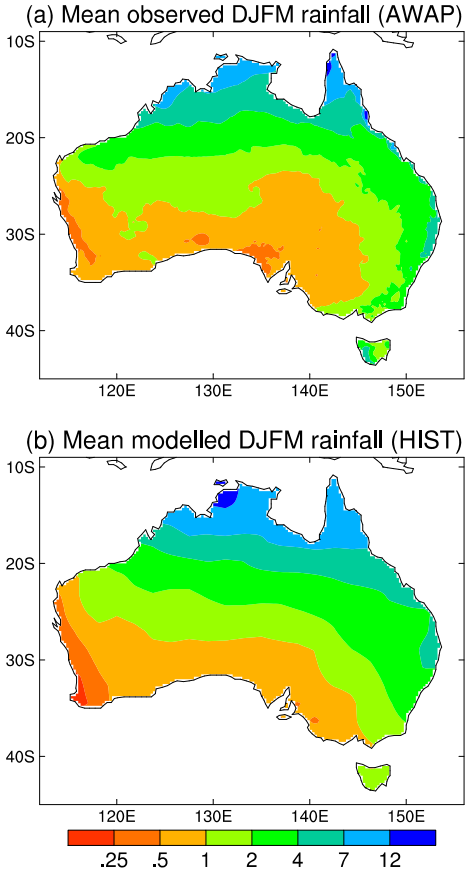

Fig. 4. DJFM rainfall, averaged over 1980 to 2005 (in mm per day): **(a)** observations from AWAP, **(b)** from the HIST ensemble mean.

ACPD
12, 5107–5188, 2012

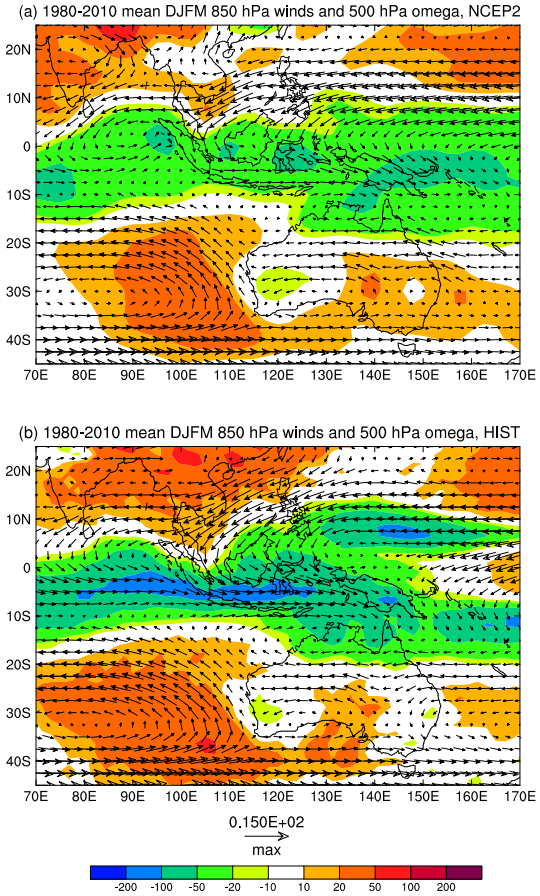

Fig. 5. Simulated mean 850 hPa wind vectors ($m\,s^{-1}$) and 500 hPa vertical velocity (shading, $hPa\,day^{-1}$) for DJFM, averaged over 1980 to 2010, **(a)** from the HIST ensemble, and **(b)** from NCEP-DOE Reanalysis 2. The maximum vector is shown below the plot.

ACPD
12, 5107–5188, 2012

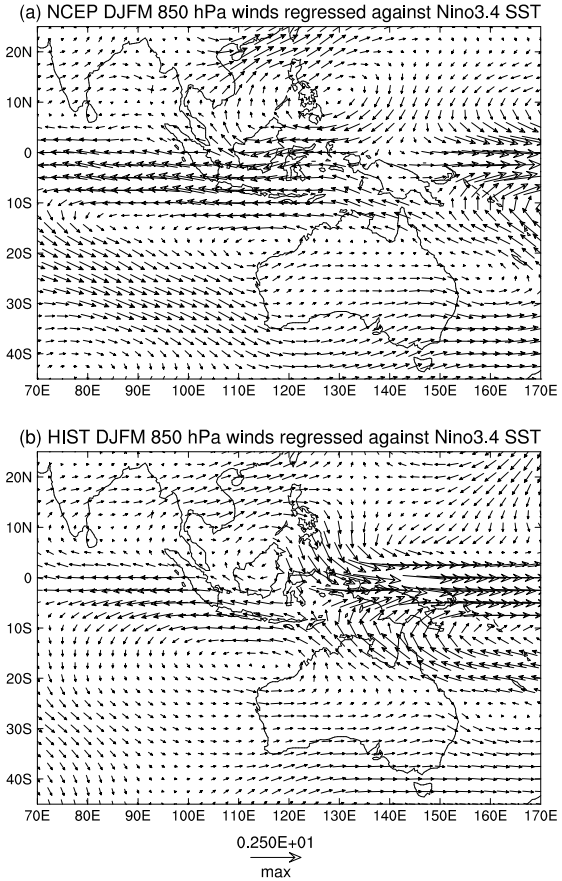

Fig. 6. DJFM 850 hPa winds regressed against Niño-3.4 SST ($m\,s^{-1}\,K^{-1}$) for the period 1951–2010, from **(a)** observations (HadISST and NCEP), and **(b)** the HIST ensemble. All data sets were linearly detrended before performing the regression.

ACPD
12, 5107–5188, 2012

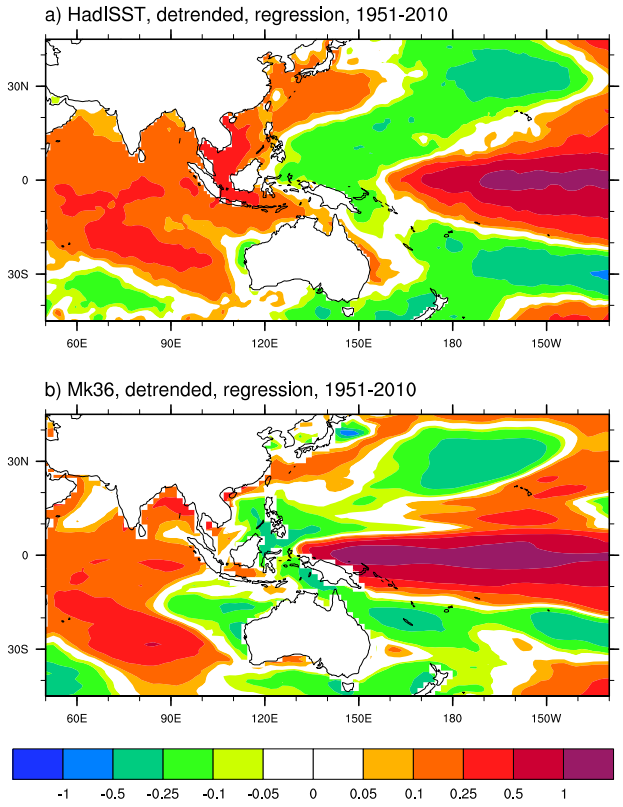

Fig. 7. DJFM gridpoint SST regressed against Niño-3.4 SST ($K\,K^{-1}$) for the period 1951–2010, from **(a)** HadISST observations, and **(b)** the HIST ensemble. Both data sets were linearly detrended before performing the regression.

ACPD
12, 5107–5188, 2012

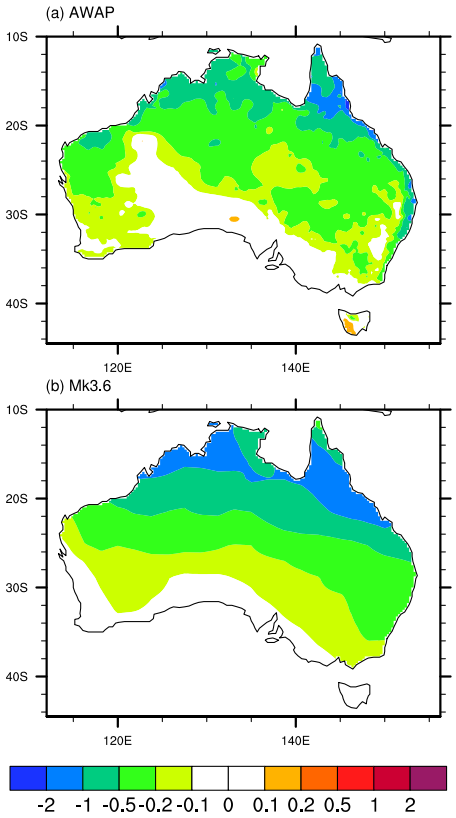

Fig. 8. DJFM rainfall regressed against Niño-3.4 SST (mm day^{-1} K^{-1}) for the period 1951–2010, from **(a)** observations (AWAP and HadISST), and **(b)** the HIST ensemble. All data sets were linearly detrended before performing the regression.

ACPD
12, 5107–5188, 2012

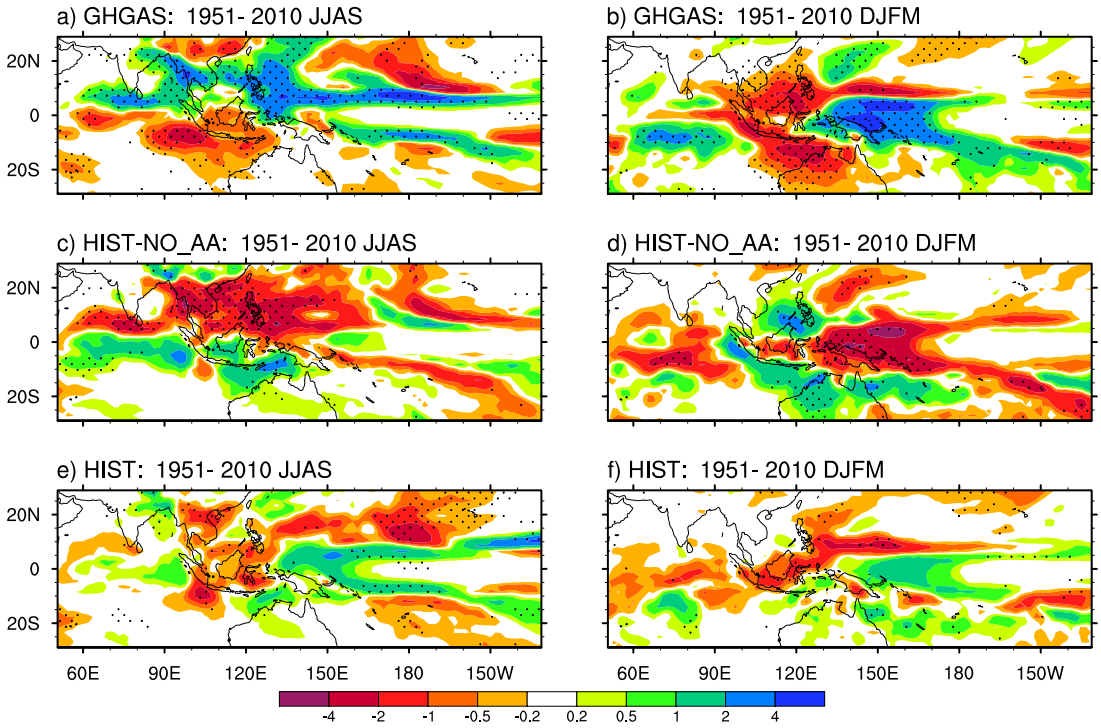

Fig. 9. Simulated rainfall trends (mm day^{-1} century^{-1}) for 1951–2010, from **(a)** GHGAS for JJAS, **(b)** GHGAS for DJFM, **(c)** HIST minus NO_AA for JJAS, **(d)** HIST minus NO_AA for DJFM, **(e)** HIST for JJAS, **(f)** HIST for DJFM . Stippled trends are significant at 5 %.

ACPD
12, 5107–5188, 2012

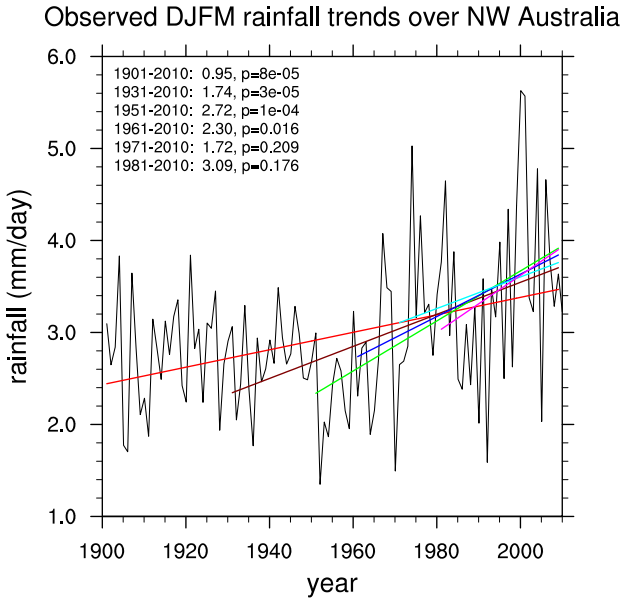

Fig. 10. Time series of observed DJFM rainfall from AWAP, averaged over land in the region 10° S to 25° S, 110° E to 135° E (shown in Fig. 1). Trend lines are fitted for the last 110, 80, 60, 50, 40 and 30 yr; the magnitude of each trend (in mm day^{-1} century^{-1}) and its level of significance are shown in the upper-left corner of the plot.

ACPD
12, 5107–5188, 2012

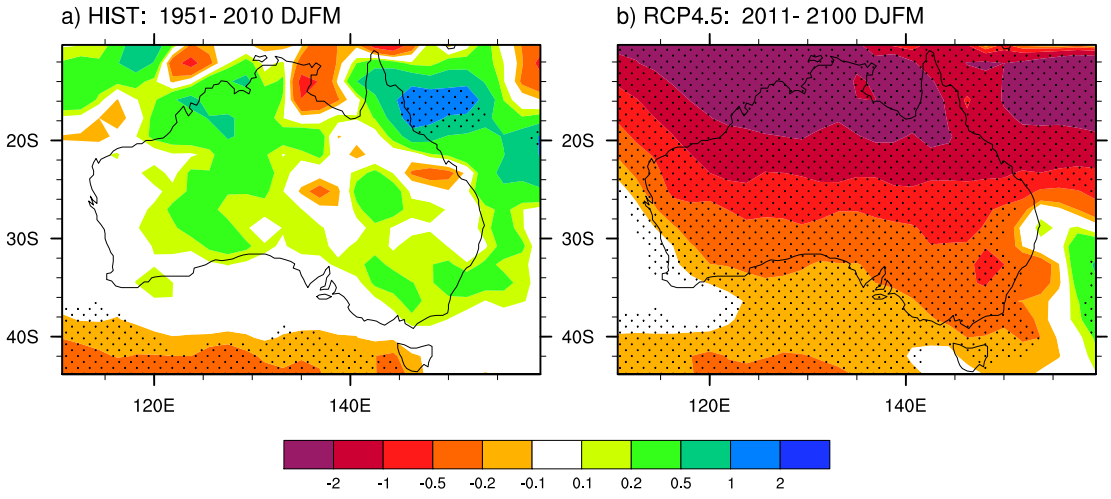

Fig. 11. Simulated DJFM rainfall trends (mm day^{-1} century^{-1}), from **(a)** HIST (1951–2010), **(b)** RCP4.5 (2011–2100). Stippled trends are significant at 5 %.

ACPD
12, 5107–5188, 2012

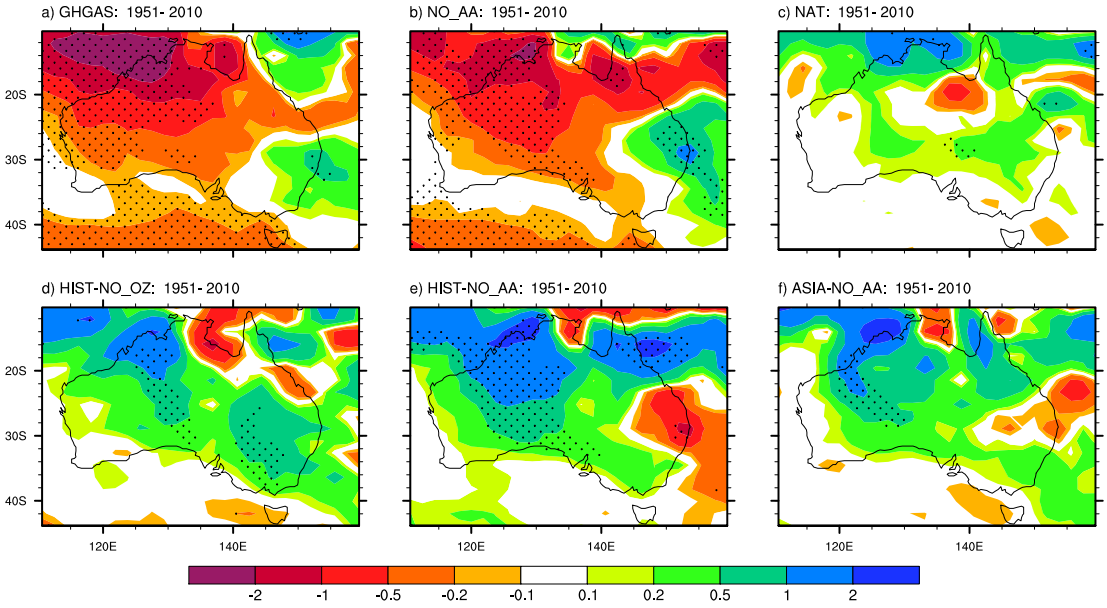

Fig. 12. Simulated DJFM rainfall trends (mm day^{-1} century^{-1}) for 1951–2010, from **(a)** GHGAS, **(b)** NO_AA, **(c)** NAT, **(d)** HIST minus NO_OZ, **(e)** HIST minus NO_AA, **(f)** ASIA minus NO_AA. Stippled trends are significant at 5 %.

ACPD
12, 5107–5188, 2012

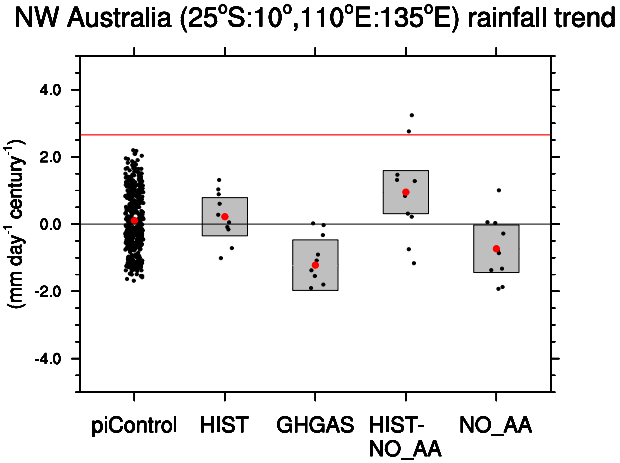

Fig. 13. 60-year DJFM rainfall trends, averaged over land in the region 10° S to 25° S, 110° E to 135° E (shown in Fig. 1). The horizontal red line shows the observed 1951–2010 trend from AWAP. The small black dots show individual 1951–2010 trends from the 10-member forced ensembles (HIST, GHGAS and NO_AA) and 440 60-yr trends from the 500-yr preindustrial control run (piControl). For the case of HIST minus NO_AA, the 10 small black dots represent trends formed by pairing run *n* of HIST with run *n* of NO_AA. The large red dots show the ensemble-mean trend from each experiment, and the grey bars show the 95 % confidence interval, based on a one-sample t-test for HIST, GHGAS and NO_AA, and two-sample t-test for HIST minus NO_AA.

ACPD
12, 5107–5188, 2012

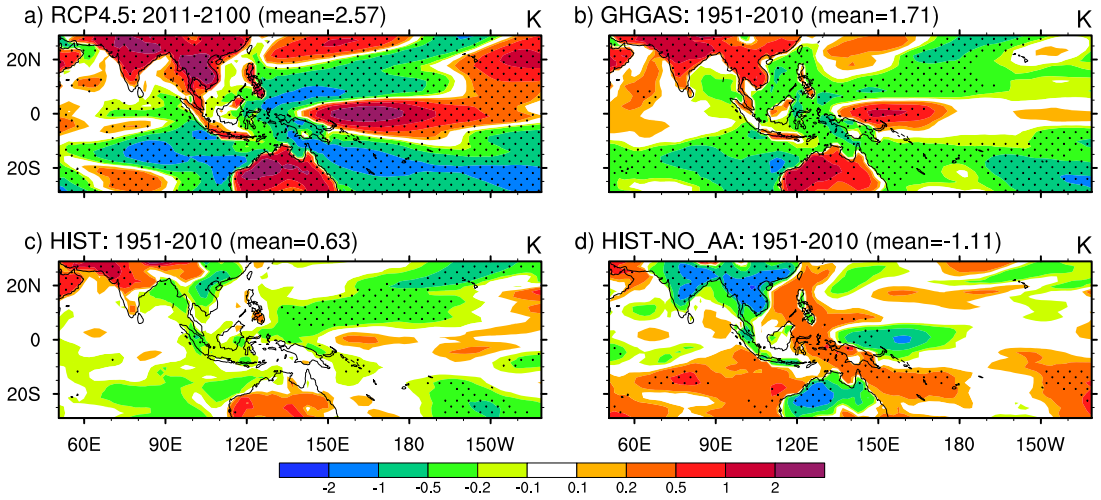

Fig. 14. Ensemble-mean DJFM trends of T_s with the low-latitude (30° S–30° N) mean T_s trend subtracted (i.e. T_{rel}), from **(a)** RCP4.5 (2011–2100), **(b)** GHGAS (1951–2010), **(c)** HIST (1951–2010), **(d)** HIST minus NO_AA (1951–2010). The low-latitude mean T_s trend for each ensemble is shown in its header (K century^{-1}). Stippled trends are significantly different from the low-latitude mean at 5 %.

ACPD
12, 5107–5188, 2012

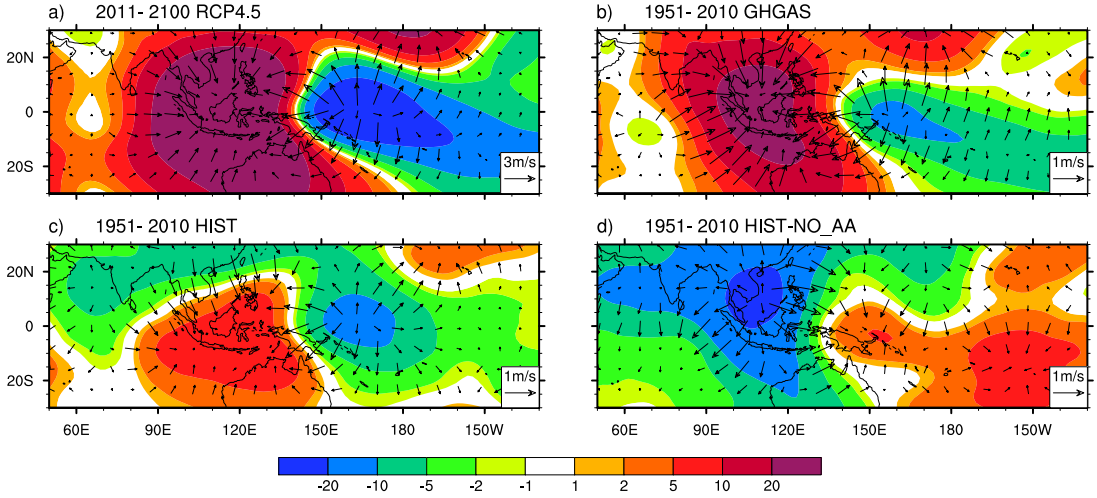

Fig. 15. Ensemble-mean DJFM trends of velocity potential (10^5 m^2 s^{-1} century^{-1}) and divergent wind vectors (m s^{-1} century^{-1}) at 200 hPa, from **(a)** RCP4.5 (2011–2100), **(b)** GHGAS (1951–2010), **(c)** HIST (1951–2010), **(d)** HIST minus NO_AA (1951–2010). The largest vector is shown in the lower-right corner of each panel; note different scaling of vectors in RCP4.5.

ACPD
12, 5107–5188, 2012

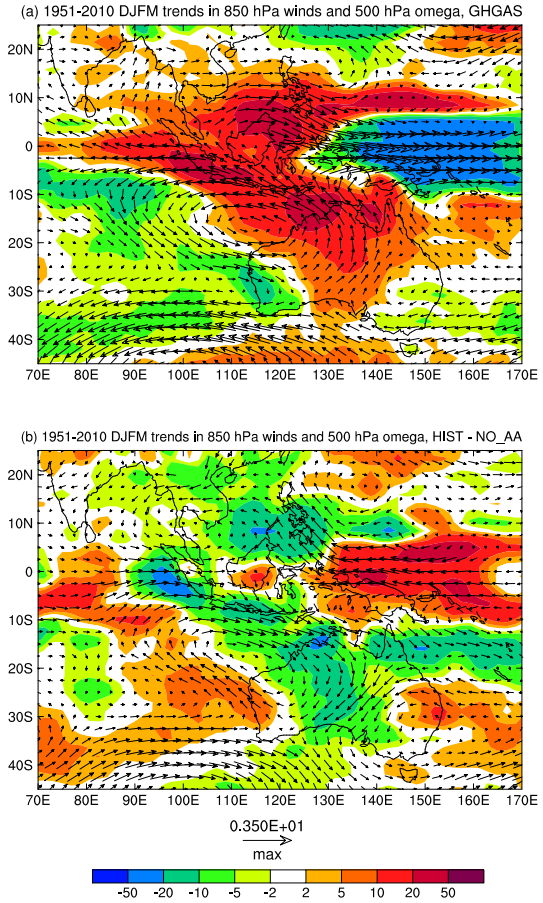

Fig. 16. Simulated 1951–2010 DJFM trends in 850 hPa wind vectors (m s^{-1} century^{-1}) and 500 hPa vertical velocity (shading, hPa day^{-1} century^{-1}), for **(a)** GHGAS, **(b)** HIST minus NO_AA. The maximum vector is shown below the plot.

ACPD
12, 5107–5188, 2012

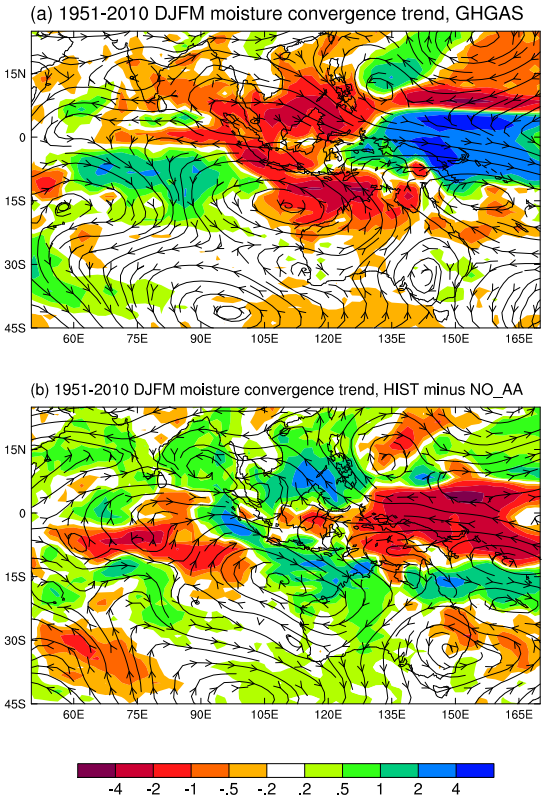

Fig. 17. Simulated 1951–2010 DJFM trends in moisture convergence (shading, in mm day^{-1} century^{-1}) and moisture transport (streamlines), for **(a)** GHGAS, **(b)** HIST minus NO_AA.

ACPD
12, 5107–5188, 2012

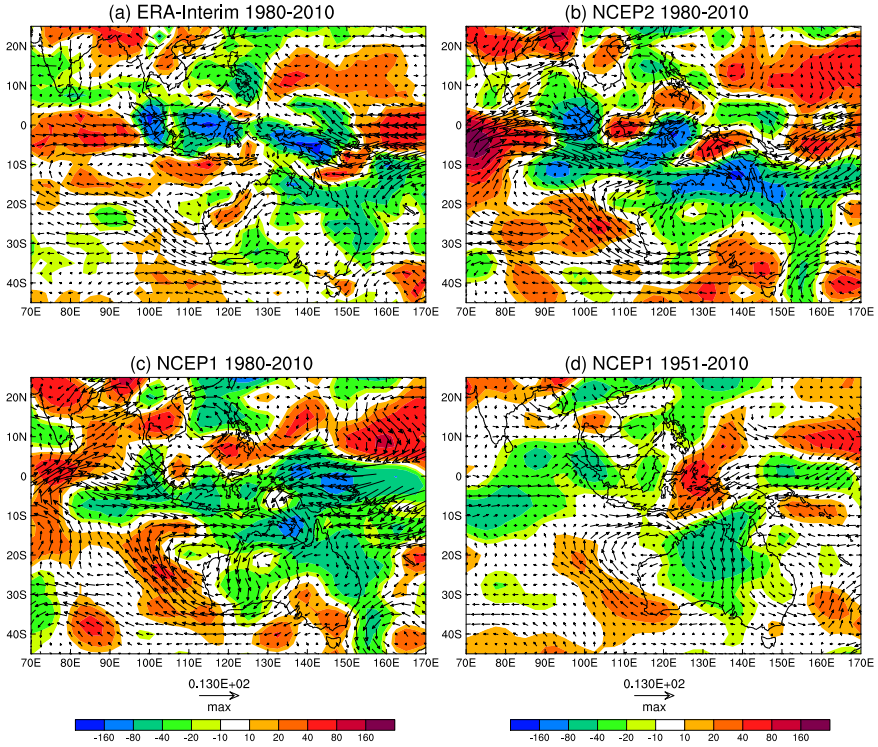

Fig. 18. Trends in 850 hPa wind vectors (m s^{-1} century^{-1}) and 500 hPa vertical velocity (shading, hPa day^{-1} century^{-1}) for DJFM from reanalyses, **(a)** 1979–2010 from ERA-Interim, **(b)** 1980–2010 from NCEP-DOE Reanalysis 2, **(c)** 1980–2010 from NCEP/NCAR Reanalysis 1, **(d)** 1951–2010 from 1980–2010 from NCEP/NCAR Reanalysis 1. The reference vector is shown at the bottom of the figure; note that scales are different from those used in Fig. 16. The ERA-Interim fields were interpolated to the 2.5° NCEP grid before plotting.

ACPD
12, 5107–5188, 2012

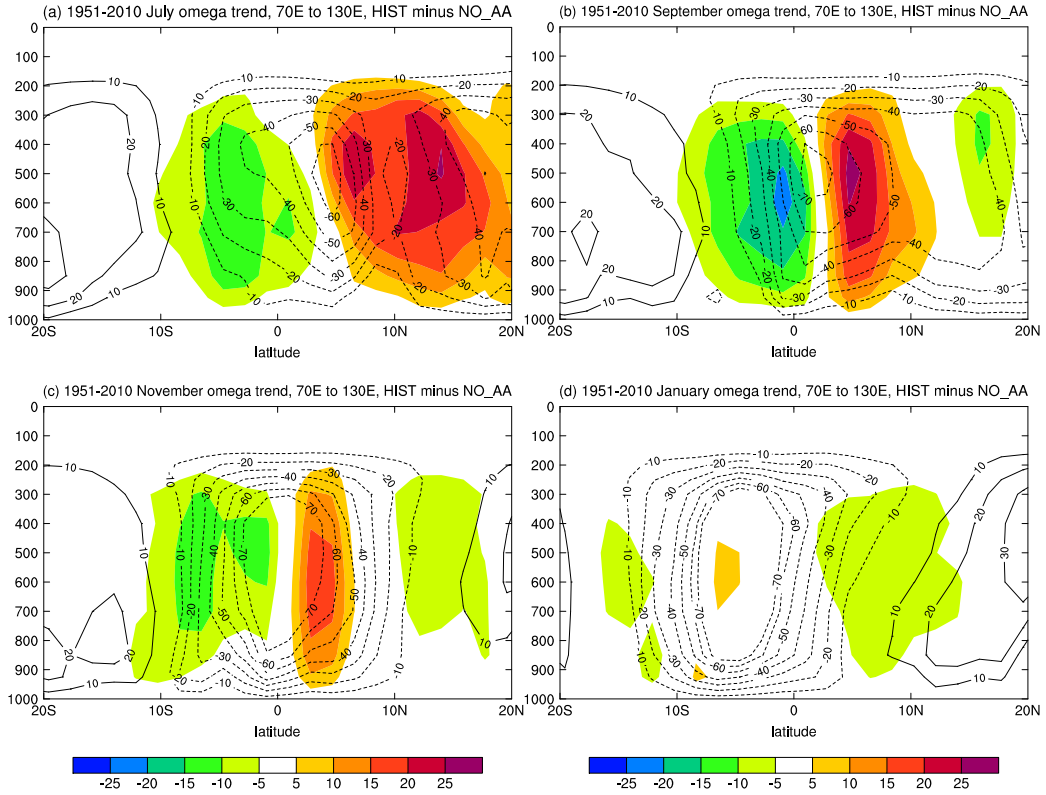

Fig. 19. 1951–2010 HIST minus NO_AA ensemble-mean trends of vertical pressure velocity, zonally averaged between 70° E to 130° E (shading, hPa day^{-1} century^{-1}) for **(a)** July, **(b)** September, **(c)** November and **(d)** January. For each month, the black contours show the mean vertical velocity field (averaged over 1970–1989 from the HIST ensemble); negative contours (denoting upward motion) are dashed. Contour interval is 10 hPa day^{-1}, with the zero contour omitted.

ACPD
12, 5107–5188, 2012

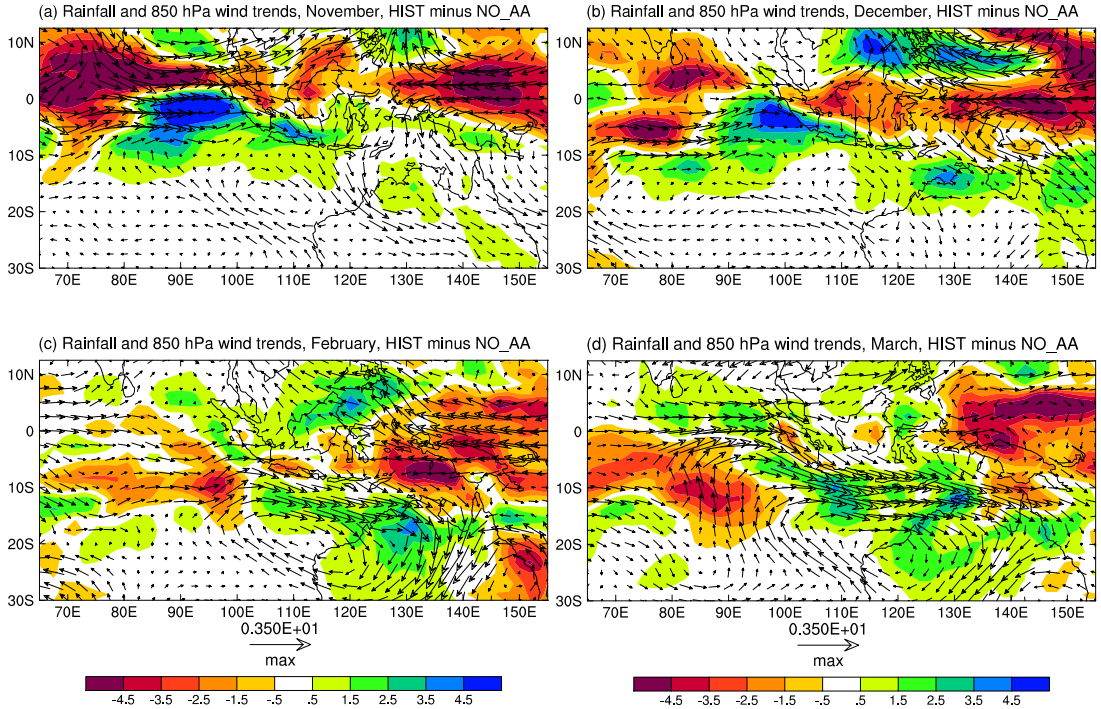

Fig. 20. 1951–2010 HIST minus NO_AA ensemble-mean trends of rainfall (shading, mm day^{-1} century^{-1}) and 850 hPa wind (vectors, m s^{-1} century^{-1}), for **(a)** November, **(b)** December, **(c)** February and **(d)** March.

ACPD
12, 5107–5188, 2012

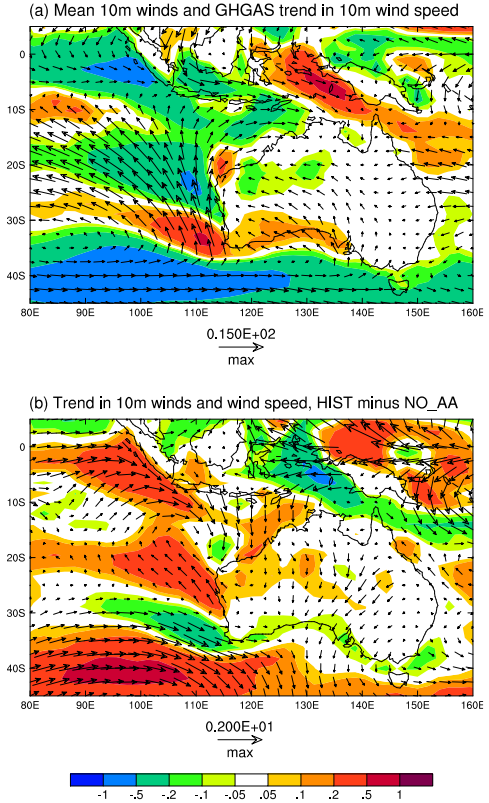

Fig. 21. 1951–2010 ensemble-mean DJFM trends of near-surface (10-m) wind speed (shaded) from **(a)** GHGAS, and **(b)** HIST minus NO_AA ($m\,s^{-1}$ $century^{-1}$). Vectors in **(a)** show mean DJFM simulated 10-m winds ($m\,s^{-1}$) for 1970–1999, and vectors in **(b)** show DJFM 10-m wind trends from HIST minus NO_AA ($m\,s^{-1}$ $century^{-1}$).

ACPD
12, 5107–5188, 2012

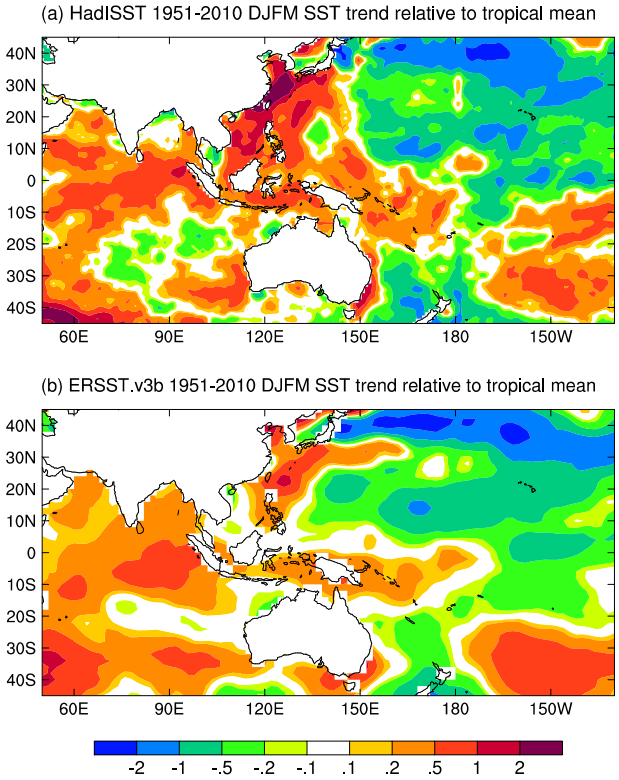

Fig. 22. Analysed DJFM SST trends for 1951–2010 with the low-latitude (30° S–30° N) mean trend subtracted (K century^{-1}), **(a)** HadISST, **(b)** ERSST.v3b.

ACPD
12, 5107–5188, 2012